

AD _____

Award Number: W81XWH-07-1-0454

TITLE: Photonic Breast Tomography and Tumor Aggressiveness Assessment

PRINCIPAL INVESTIGATOR: Swapan K. Gayen, Ph. D.

~~RESEARCH INSTITUTE FOR MEDICAL PHYSICS
UNIVERSITY OF TORONTO
144 College Street
Toronto, Ontario
M5S 2M2~~

CONTRACTING ORGANIZATION: Research Foundation of CUNY
New York, NY 10019-2925

Á

REPORT DATE: July 201G

Á

TYPE OF REPORT: Annual Summary

Á

PREPARED FOR: U.S. Army Medical Research and Materiel Command
Fort Detrick, Maryland 21702-5012

DISTRIBUTION STATEMENT: Approved for Public Release;
Distribution Unlimited

The views, opinions and/or findings contained in this report are those of the author(s) and should not be construed as an official Department of the Army position, policy or decision unless so designated by other documentation.

REPORT DOCUMENTATION PAGE

Form Approved
OMB No. 0704-0188

Public reporting burden for this collection of information is estimated to average 1 hour per response, including the time for reviewing instructions, searching existing data sources, gathering and maintaining the data needed, and completing and reviewing this collection of information. Send comments regarding this burden estimate or any other aspect of this collection of information, including suggestions for reducing this burden to Department of Defense, Washington Headquarters Services, Directorate for Information Operations and Reports (0704-0188), 1215 Jefferson Davis Highway, Suite 1204, Arlington, VA 22202-4302. Respondents should be aware that notwithstanding any other provision of law, no person shall be subject to any penalty for failing to comply with a collection of information if it does not display a currently valid OMB control number. **PLEASE DO NOT RETURN YOUR FORM TO THE ABOVE ADDRESS.**

Table of Contents

	Page
Cover.....	1
SF 298.....	2
Table of Contents.....	3
Introduction.....	4
Body.....	4
Key Accomplishments.....	14
Reportable Outcomes.....	14
Conclusions.....	15
References.....	15
Appendices.....	17

4. INTRODUCTION

This document presents the research activities pursued during the *fifth* reporting period (June 15, 2011 – June 14, 2012) of the project, “*Photonic Breast Tomography and Tumor Aggressiveness Assessment*.” The major thrust was on developing fast, accurate, and noninvasive methods for detecting and locating breast tumors in early growth stages when those are more amenable to treatment. We continued developing and testing the near-infrared (NIR) light-based experimental methods that capitalize on intrinsic differences in optical absorption and scattering properties of normal and cancerous breast tissues. We have further initiated the development of fluorescence tomography approaches that uses exogenous contrast agents to enhance contrast and hold potential for functional and molecular imaging.

5. BODY

During this reporting period we have built on our earlier research on the project [1-4] and made substantial progress in developing and testing ***non-invasive near-infrared optical imaging modalities for early detection of breast cancer*** [Specific Aim 4]. Our focus has been on developing non-iterative approaches to realize fast, near-real-time image reconstruction of small targets. Early detection of breast tumor with requisite sensitivity and specificity is a challenging undertaking and we continued developing and testing different approaches. We have initiated development of numerical algorithms for fluorescence tomography, since it has the potential to provide higher contrast as well as molecular and functional information through the use of exogenous fluorophores. In particular, we pursued the following tasks:

- *Comparison of the efficacy of diffuse optical tomography using different Decomposition Methods;*
- *Developing Time Reversal Optical Tomography (TROT) for extended targets; and*
- *Developing Fluorescence Tomography.*

We provide a brief outline of activities and accomplishments in these areas, and refer to appended materials for detailed description where applicable.

5.1. Diffuse Optical Imaging Using Decomposition Methods

Diffuse optical imaging (DOI) for detection and retrieval of location information of targets in a highly scattering turbid medium may be treated as a “blind source separation” (BSS) problem [5]. BSS is a general problem in information theory that involves retrieval of “component” signals from measured signals. The measured signals are weighted mixtures of the component signals contributed by the targets (“blind sources”) and may be expressed as a matrix equation:

$$X = AS, \quad (1)$$

where rows of X represent the measured mixed signals, rows of S represent the component signals, and A is the mixing matrix.

Different matrix decomposition methods, such as, Independent Component Analysis (ICA) [6], Principal Component Analysis (PCA) [7] and Non-negative Matrix Factorization (NMF) [8] are used to solve the general BSS problem. The three algorithms have different assumptions, which may lead to different favored conditions. We introduced these decomposition methods for solving the diffuse imaging problem, and carried out a systematic study using simulated and

experimental data to compare the performance of the three decomposition methods – ICA, PCA, and NMF [9, 10]. We first reported the initial results of this comparative study in our fourth Annual Report [4]. The study involved detection and retrieval of three-dimensional (3-D) location information of *absorptive* and *scattering* targets in a model medium whose thickness and optical absorption coefficient, scattering coefficient, transport length, and anisotropy factor were similar to the average values of those parameters for a compressed human breast. The key result was that the approaches could detect and extract 3-D location of small tumor-like targets within ~ 2 mm of their known locations. The formalism and some results were presented in the fourth Annual Report [4], and in the first part of this reporting period we published a peer-reviewed journal article [10] presenting the experimental methods, materials, algorithms, and key results, which is appended (*Appendix 1*) to this report for further details.

It was apparent from our work on absorptive and scattering targets that the NMF formalism, because of its non-negativity constraint, may be particularly suited for detection of fluorescent targets. We explored development of fluorescence tomography (Section 5.3) during the later part of the reporting period.

5.2. Time Reversal Optical Tomography (TROT) for Extended Targets

Earlier we reported on our development of *Time Reversal Optical Tomography* (TROT) for detecting and obtaining 3-D location information about small, point-like absorptive and scattering targets [2-4, 11] as a part of our on-going quest for fast and accurate methods for detection and localization of tumours in breast, and for detection of margins during surgical removal of breast tumours (*Specific Aim 4*). The approach combines the idea of time reversal (TR) invariance and the vector subspace classification method of Multiple Signal Classification (MUSIC). It provided the locations of small absorptive and scattering targets within a turbid medium with high accuracy [11]. During the current reporting period we focused on further developing the approach to encompass extended targets and to assess their size, and some measure of optical properties. These assessments are necessary for target identification, such as, classifying a growth in the breast as benign or malignant. We test the formalism so developed using simulated data for a single absorptive target, a single scattering target, and two absorptive targets assuming different noise levels. Here we present a brief overview of the TROT formalism for small targets [11], outline how the size and optical strength of an extended target may be estimated, and defer the details to an appended conference proceedings paper (*Appendix 2*).

In the first order Born approximation, the perturbation in the light intensity distribution due to the presence of the targets (inhomogeneities in optical properties) can be expressed using a data matrix [11] of the form:

$$K \approx \left\{ \sum_{m=1}^M G^d(r_i, \mathbf{X}_m) \tau_m G^s(\mathbf{X}_m, \mathbf{r}_j) \right\} = \sum_{m=1}^M g_d(\mathbf{X}_m) \tau_m g_s^T(\mathbf{X}_m), \quad (2a)$$

for *absorptive* targets, and

$$K \approx \sum_{m=1}^M \sum_{\alpha=\{x,y,z\}} \partial_\alpha g_d(\mathbf{X}_m) \tau_m \partial_\alpha g_s^T(\mathbf{X}_m), \quad (2b)$$

for *scattering* targets, where $g_s(\mathbf{r}) = \{G^s(\mathbf{r}, \mathbf{r}_j), j = 1, \dots, N_s\}$ and $g_d(\mathbf{r}) = \{G^d(\mathbf{r}_i, \mathbf{r}), i = 1, \dots, N_d\}$ are the Green's function vectors (GFVs) associated with the source and detect planes, respectively; the superscript T denotes transpose; $G^s(\mathbf{r}, \mathbf{r}_s)$ and $G^d(\mathbf{r}_d, \mathbf{r})$ are the Green's functions

that describe light propagations in the background medium from a source at \mathbf{r}_s to a target (inhomogeneity) at \mathbf{r} and from the target to a detector at \mathbf{r}_d , respectively; $\tau_m = \delta\mu_a(\mathbf{X}_m)c\delta V_m$ ($\tau_m = \delta D(\mathbf{X}_m)c\delta V_m$) is the absorptive (scattering) optical strength of the m^{th} absorptive (scattering) target at \mathbf{X}_m with volume δV_m ; $\delta\mu_a$ (δD) is the difference in the absorption (diffusion) coefficients between the target and the background medium; N_s , N_d and M are the numbers of sources, detectors and targets, respectively. It is assumed the number of targets is less than the number of sources and detectors, $M < \min(N_d, N_s)$; c is the light speed in the medium. A time reversal matrix is constructed as $T_{SDDS} = K^{\dagger}K$ [$T_{DSSD} = (K^T)^{\dagger}K^T = K^*K^T$] in frequency domain, and $T_{SDDS} = K^T K$ ($T_{DSSD} = K K^T$) in the continuous wave illumination. T_{DSSD} and T_{SDDS} have a common set of eigenvalues $\{\lambda_j, j = 1, \dots, \min(N_s, N_d)\}$, and different sets of eigenvectors $\{u_i, i = 1, \dots, N_d\}$ and $\{v_j, j = 1, \dots, N_s\}$, respectively. The eigenvectors are separated into signal and noise subspaces using an L -curve method [12] with an eigenvalue threshold ε . For absorptive targets, the locations are determined using the MUSIC pseudo spectrum [11]

$$P_s(\mathbf{X}_p) = \left\| g_s(\mathbf{X}_p) \right\|^2 \left/ \left\| g_s(\mathbf{X}_p) \right\|^2 - \sum_{\lambda_j > \varepsilon} |v_j^T g_s(\mathbf{X}_p)|^2 \right\|, \quad (3a)$$

associated with the source plane or a similar form for the detector plane $P_d(\mathbf{X}_p)$, or the product of these two,

$$P(\mathbf{X}_p) = P_s(\mathbf{X}_p)P_d(\mathbf{X}_p), \quad (3b)$$

where \mathbf{X}_p is a test target position in the sample volume. Since the eigenvalues and eigenvectors of T_{SDDS} and T_{DSSD} can be connected using singular value decomposition (SVD), *i.e.*

$$K \approx U \Sigma V^T, \quad (4)$$

where $V = \{v_j\}$ and $U = \{u_i\}$, corresponding to $\Sigma = \text{diag}\{\sqrt{\lambda_j} > \varepsilon\}$, are matrices for the signal subspaces. By comparing Eq. (4) and Eq. (2), the target optical property can be retrieved by transforming the eigenvalue matrix Σ via

$$\Gamma \approx (\mathbf{G}^d)^{-1} U \Sigma V^T ((\mathbf{G}^s)^T)^{-1}, \quad (5)$$

where $\Gamma = \text{diag}\{\tau_m, m = 1, \dots, M\}$; $\mathbf{G}^s = \{g_s(\mathbf{r}_m)\}$, $\mathbf{G}^d = \{g_d(\mathbf{r}_m)\}$ are matrices including GFVs associated with the retrieved target positions. For scattering targets, the GFVs g_d and g_s in Eq.(3) and Eq.(5) are replaced by $\partial_\alpha g_d$ and $\partial_\alpha g_s$, $\alpha = x, y, z$, respectively.

An optimal contour (a surface Ω when plotted in 3D) in the pseudo spectrum is selected to be the boundary of the target(s), via [13]

$$\Omega = \arg \min_{\Omega} \|K - K_{\text{cal}}(\Omega)\|^2, \quad (6)$$

where K is normalized data matrix obtained from known target surface in simulation (from experimental measurements for real targets) and $K(\Omega)$ is normalized data matrix calculated from the contour of the pseudo spectrum. The Green's functions used in the calculation are those for the intervening medium.

In the simulation to test the formalism, the sample was taken to be a 40-mm thick uniform scattering slab with lateral dimension of 80 mm \times 80 mm. Its absorption and diffusion

coefficients were assumed to be $\mu_a = 0.003 \text{ mm}^{-1}$ and $D = 1/3 \text{ mm}$ (transport mean free path, $l_t = 1 \text{ mm}$), respectively, which are similar to the average value of those parameters for human breast tissue. The index of refraction n of the medium was taken to be 1.33. The speed of light is $2.998 \times 10^8 \text{ m/s}$, or 299.8 mm/ns in vacuum, and 225.4 mm/ns in the medium. Three simulated datasets were generated with 10-mm diameter spherical targets embedded. In the first dataset, an absorptive target was centered at $(40, 40, 20) \text{ mm}$. In the second dataset, two absorptive targets were located at $(20, 40, 20) \text{ mm}$ and $(60, 40, 20) \text{ mm}$, respectively. In the third dataset, a scattering target was centered at $(40, 40, 20) \text{ mm}$. The absorption coefficient of all the absorptive targets was set to be higher than the background with $\Delta\mu_a = 0.001 \text{ mm}^{-1}$, while the diffusion coefficient was taken to be the same as that of background. The diffusion coefficient of the scattering target was set to be lower than the background (higher scattering coefficient) with $\Delta D = -0.1 \text{ mm}$ ($l_t = 0.7 \text{ mm}$), while the absorption coefficient was taken to be the same as that of the background. The volume of all targets was 515 mm^3 when the sample volume is discretized into $1 \text{ mm} \times 1 \text{ mm} \times 1 \text{ mm}$ voxels in the forward model. The optical strength of the absorptive targets was $\Delta\mu_a c \Delta V = 116.08 \text{ mm}^3/\text{ns}$; while the optical strengths of the scattering target was $\Delta D c \Delta V = -11608.1 \text{ mm}^5/\text{ns}$. The incident CW beam step scanned the sample at 41×41 grid points covering an $80 \times 80 \text{ mm}^2$ area, with a step size of 2 mm. Light on the opposite side was recorded at 41×41 grid points covering the same area. Additive Gaussian noise of different noise levels was added to the simulated data. The data matrix K was then obtained using Eq. (2) directly, and analyzed using the TROT formalism. The results are shown below. For simplicity, when the reconstruction result for one target is displayed, a smaller volume of $40 \text{ mm} \times 40 \text{ mm} \times 40 \text{ mm}$ around the center is selected. Due to the distortion in the retrieved target shape, target volume will be used to describe the target size.

Results for the three different sets of targets are detailed in *Appendix 2*. Here we present the result for the case of two spherical absorptive targets (diameter 10 mm) embedded in the medium, with a center-to-center separation of 40 mm. Different added noise levels: 0%, 5%, 10%, 20%, and 100% were considered. The target locations of two targets were accurately found to be $(20, 40, 20) \text{ mm}$ and $(60, 40, 20) \text{ mm}$ at all noise levels. Typical axial and sagittal images of the targets generated using the pseudo spectra for a noise level of 20% are displayed in Fig. 1. Similar images were obtained for other noise levels. The optical strength of each target was calculated within 3.3% error at all noise levels. The size of targets was found within 13.4% error when no noise was present, and varied with noise added. The retrieved optical strength and size of the targets are listed in Table I for different noise levels. Since both targets have the same optical property and size in the simulated data and the retrieved data, only one set of values is shown in the table.

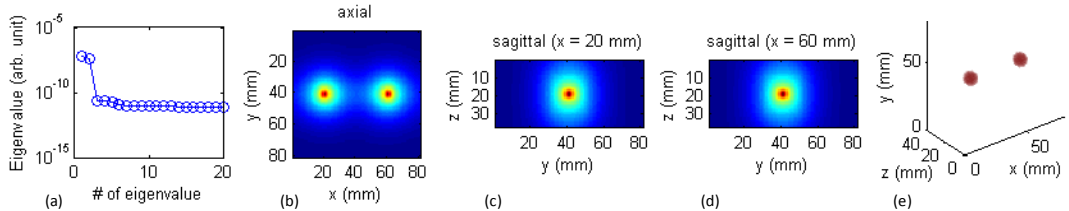


Fig.1. (a) Eigenvalues plotted in logarithmic scale; (b), (c) and (d) are the axial and sagittal views of the targets using pseudo spectrum in logarithmic scale; (e) is the retrieved target image. The added noise level was 20%.

Further simulations (not shown here) indicate that retrieved target size was more accurate when small targets were involved. Simulations with one target at different locations and two targets with different separations were also tested for absorptive and scattering targets. The target locations were accurately retrieved in all of these cases. The retrieved optical strength in all cases was much less sensitive to the target location and size than the retrieved target size. As expected, it was more challenging to retrieve the optical strength and size of scattering targets than absorptive targets.

Table I. Optical strength and size of two absorptive targets (10-mm diameter)

Noise Level (%)	Optical Strength		Size	
	Retrieved (mm ³ /ns)	Error (%)	Retrieved (mm ³)	Error (%)
0	112.3	3.3	584	13.4
5	112.3	3.3	295	42.7
10	112.3	3.3	368	28.5
20	112.3	3.3	487	5.4
100	112.2	3.3	663	28.7

* Known values: volume: 515 mm³, optical strength: 116.08 mm³/ns

Further simulations also showed closer distance between two targets made target size retrieval more difficult, because of the cross talk between the two targets showing up in the contour of the pseudo spectrum.

Future work will involve testing the efficacy of the approach using experimental data for targets of different size and optical strength with optical properties similar to that of breast tumors at different stages.

5.3. Fluorescence Tomography

Diffuse optical imaging approaches for breast cancer detection may be developed capitalizing on the absorption, scattering, and fluorescence contrasts between the tumor and the surrounding tissues. However, there has been a recent surge in interest in fluorescence tomography because of its superior detection sensitivity and specificity, higher signal-to-background ratio and better spatial resolution than other diffuse optical imaging (DOI) approaches, and potential to provide molecular information on disease-induced changes in biological tissues [14-16]. In addition, advances towards development of target-specific exogenous contrast agents [16, 17], imaging instrumentation [18, 19], as well as, analytical methods and numerical algorithms [15, 20] hold the promise for noninvasive detection and characterization of tumors. The use of target-specific contrast agent endows fluorescence tomography with potentially higher contrast, and specificity. The key attributes of a clinically useful cancer imaging modality include early detection, adequate spatial resolution, speedy image reconstruction, and diagnostic potential. Fluorescence-based approaches are sensitive to molecular changes and may provide useful diagnostic information, but diffuse nature of light propagation in biological tissues impedes spatial resolution. For these reasons, we initiated the development of fluorescence tomography towards the end of the current reporting period.

We plan to develop fluorescence tomography approaches based on the TROT and NMF, which we previously explored and tested for absorptive and scattering targets [11, 9]. While other

fluorescence tomography approaches are computation intensive since those try to iteratively compute fluorescence properties (such as, fluorophore concentration) of every voxel of the sample volume, both TROT and NMF are non-iterative and are expected to provide faster localization. During this reporting period we started developing the algorithm for fluorescence TROT and used it with experimental data for detecting and locating a single fluorescent target in a breast simulating turbid medium.

The experimental arrangement uses a multi-source illumination and multi-detector signal acquisition scheme to acquire multiple angular views of the sample. The input surface (source plane) of the slab sample is scanned across an external point light source (laser beam). The fluorescent target(s) embedded in the highly scattering medium are excited by diffusely propagating light of wavelength λ_x . A fraction of the forward propagating fluorescence signal emitted by the targets at wavelength λ_m , is detected on the other side of the sample by a two-dimensional detector array. For small fluorescent targets at \mathbf{r}_j with volume V_j , the fluorescence signal from the target at \mathbf{r} illuminated by a point source of unit power at \mathbf{r}_s is given by[20]

$$K = \sum_j g_d(\mathbf{r}_j, \omega) f_j(\omega) g_s^T(\mathbf{r}_j, \omega), \quad (7)$$

where $g_s(\mathbf{r}, \omega) = \{G_x(\mathbf{r}, \mathbf{r}_s, \omega)\}^T$ and $g_d(\mathbf{r}, \omega) = \{G_m(\mathbf{r}_d, \mathbf{r}, \omega)\}^T$, (the superscript T denotes transpose); $G_x(\mathbf{r}, \mathbf{r}_s, \omega)$ is a Green's function that describes the propagation of excitation light at excitation wavelength λ_x from the source at \mathbf{r}_s to the target at \mathbf{r} ; $G_m(\mathbf{r}_d, \mathbf{r}, \omega)$ is a Green's function that describes the propagation of the fluorescent light at emission wavelength λ_m from the target at \mathbf{r} to the detector at \mathbf{r}_d ; ω is the modulation angular frequency of the light; $f_j(\omega)$ is the fluorescence strength of the j^{th} target, given by

$$f_j(\omega) = \gamma(\mathbf{r}_j) c_m V_j / [1 - i\omega\tau(\mathbf{r}_j)], \quad (8)$$

γ is the fluorescence yield, c_m is the speed of light in the medium, and τ is the fluorescence lifetime. K describes that the diffuse propagation of excitation light of wavelength, λ_x from the sources through the medium to illuminate the targets, and then the propagation of emitted fluorescence of wavelength, λ_m from the targets to the detectors. In this study, continuous wave (CW) illumination is used, *i.e.* $\omega = 0$. A time reversal matrix $T_{SDDS} = K^T K$ ($T_{DSSD} = K K^T$) is constructed. A set of eigenvectors $\{u_k, k = 1, \dots, N_d\}$ and $\{v_l, l = 1, \dots, N_s\}$ are calculated for T_{DSSD} and T_{SDDS} , respectively, with common eigenvalues $\{\mu_j, j = 1, \dots, \min(N_s, N_d)\}$, where N_s and N_d are numbers of sources and detectors, respectively[11]. The eigenvalues $\mu_j = |f_j|^2 \|g_d(\mathbf{r}_j, \omega)\|^2 \|g_s(\mathbf{r}_j, \omega)\|^2$ are proportional to squared fluorescence strengths of the targets if the targets are well resolved; otherwise, they are linear combinations of individual fluorescence strengths of different targets [11].

By using an L -curve method with an eigenvalue threshold ε [12], eigenvectors are separated into signal and noise subspaces. A pseudo spectrum associated with detector plane is calculated using multiple signal classification (MUSIC) for a test target position \mathbf{X}_p in the sample volume [11]

$$P_d(\mathbf{X}_p, \omega) = 1 / \sum_{\mu_j < \varepsilon} \left| \mathbf{u}_j^T \frac{g_d(\mathbf{X}_p, \omega)}{\|g_d(\mathbf{X}_p, \omega)\|} \right|^2. \quad (9)$$

The locations of targets are retrieved to be the poles of the pseudo spectrum. A similar pseudo spectrum for the source plane,

$$P_s(\mathbf{X}_p, \omega) = 1 \left/ \sum_{\mu_j < \varepsilon} \left| v_j^T \frac{g_s(\mathbf{X}_p, \omega)}{\|g_s(\mathbf{X}_p, \omega)\|} \right|^2 \right. . \quad (10)$$

or for both source and detector planes

$$P(\mathbf{X}_p, \omega) = 1 \left/ \sum_{\mu_j < \varepsilon} \left(\left| u_j^T \frac{g_d(\mathbf{X}_p, \omega)}{\|g_d(\mathbf{X}_p, \omega)\|} \right|^2 + \left| v_j^T \frac{g_s(\mathbf{X}_p, \omega)}{\|g_s(\mathbf{X}_p, \omega)\|} \right|^2 \right) \right. . \quad (11)$$

may also be used to retrieve the target position.

The sample used in the experiment to demonstrate the approach was a 250 mm \times 250 mm \times 60 mm rectangular transparent plastic cell filled with Intralipid-20% (Baxter) suspension in distilled water with a fluorescent targets embedded inside. The thickness of the sample was comparable to that of a typical compressed breast. The concentration of Intralipid-20% was adjusted[21] to provide a transport mean free path l_t of \sim 1mm, which happens to be about the same for both excitation and emission wavelengths, and was similar to the average value of l_t for human breast tissue at these wavelengths. The fluorescent target was a 4.2 mm inner-diameter 10-mm long cylindrical glass tube filled with solution of ICG dye (Sigma-Aldrich) water. The dye solution in the targets was prepared by dissolving ICG at a concentration of 1 μ M in the Intralipid-20% suspension of same concentration as the background medium to ensure that the target had the same scattering coefficient as the background medium, but a higher absorption coefficient of 0.027 mm^{-1} . The water solution of ICG absorbs light over the 600 – 900 nm range with peak at 780 and fluoresces in the 790 – 966 nm range with peak at around 825 nm in the NIR enabling deeper penetration of light in tissues. It has been approved by Food and Drug Administration (FDA) for biomedical applications.

The experimental arrangement is shown schematically in Fig. 2 (*Specific Aim 4, Task 14*). The target was embedded in the mid-plane ($z = 30$ mm) of the sample cell. A multi-source sample excitation and multi-detector fluorescence signal acquisition scheme was used to acquire multiple angular views of the sample.

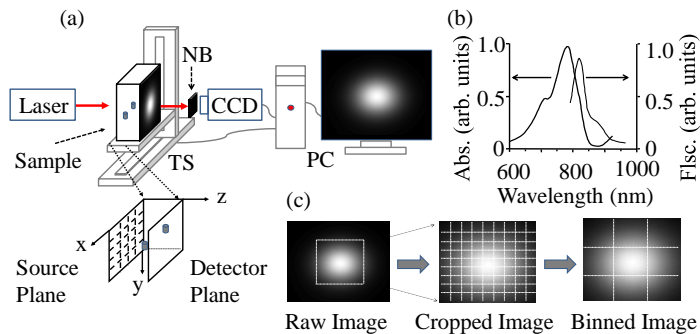


Fig.2. (a) A schematic diagram of the experimental arrangement for imaging objects embedded in a turbid medium. [Key: NB = narrow band pass filter, TS = translational stage, CCD = charge coupled device, PC = personal computer] Inset (below) shows the 2-D array in the input plane that was scanned across the incident laser beam and a typical raw image is shown in the PC monitor. (b) The absorption and fluorescence spectra of ICG in water. (c) A typical raw image is cropped and binned.

The entrance face of the slab sample (*source plane*) was illuminated by a 100-mW 790-nm diode laser beam. The multi-source illumination scheme was realized by scanning the sample across the laser beam in a two-dimensional *x*-*y* array of 9 x 9 grid points with a 5-mm step size using a computer-controlled translation stage. A cooled CCD camera equipped with a 60-mm focal-length camera lens collected and sensed a fraction of the forward propagating fluorescence signal from the opposite face of the sample (*detection plane*) through a narrow-band (full-width-at- half-maximum (FWHM) bandwidth of 10 nm) interference filter with 50% peak transmission at 830 nm. The CCD camera had 1024×1024 pixels with a pixel size of 24 μm , and was considered as multi-detector, since each illuminated pixel could be considered as an individual detector. The NB filter was chosen to select a substantial fraction of the ICG fluorescence around the peak emission wavelength and block the transmitted 790 nm pump light. The scanning and data acquisition processes were controlled by a personal computer (PC). Raw images were recorded by the PC for each scan position, and stored for subsequent analysis. A typical image, which is a 2-*D* intensity distribution, is shown in the left frame of Fig. 2(c).

At every scan position, an image was also acquired with the NB filter removed. In this case, the recorded images were essentially transillumination images since the fluorescence signal was negligible compared to the much more intense transmission signal (ratio of transmission signal to fluorescence signal ~ 1500). Thus correlated imaging and retrieval of target location using both fluorescence and transmission measurements were enabled in this experiment. The transmission images were analyzed to estimate the average value of the optical property of the medium $\kappa = (3\mu_a\mu_s')^{1/2}$, where μ_a and μ_s' are the absorption and reduced scattering coefficients at 790 nm, respectively. In fact, the values of these optical parameters of Intralipid-20% suspension in water happened to be very close for excitation and fluorescence wavelengths.

From each fluorescence image, a region of interest was cropped out and every 5×5 pixels in the cropped image were binned to one pixel to enhance the signal-to-noise ratio. The response data matrix was constructed using the transmitted fluorescence light intensity distribution in the processed images. The TR matrix was generated by multiplying the response matrix by its transpose for our CW probing scheme. The eigenvalue equation of TR matrix was solved. Then the signal and noise subspaces were separated. MUSIC pseudo spectrum was calculated and target locations were determined using the poles in the pseudo spectrum.

For comparison, the transmission data were also analyzed using TROT as detailed in Ref. 11. In this case, the target was absorptive, and the contrast was mainly due to higher absorption of the excitation beam by the target. It should be noted that absorption measurement involves changes in the intensity of the excitation beam, and consequently the TROT analysis used the difference images between the raw transmission images and a reference image for the background medium. The reference image may be estimated as the average of the images acquired at all scan positions.

The TR matrix was constructed using the fluorescence data, and an eigenvalue equation was then solved. The eigenvector with the dominant eigenvalue was used to calculate the pseudo spectrum for all voxels in the 3-*D* space of the sample. The voxel size was 0.77 mm \times 0.77 mm \times 1 mm. Three-dimensional tomographic pseudo images were generated using the pseudo spectrum. The single target was detected, and the position of the target was determined using the peak in the pseudo spectrum and listed in Table II, with comparison to the actual position. The image at the retrieved *z*-coordinate of the target position (*z* = 30.5 mm) plotted using the pseudo spectrum is shown in Fig. 3(a).

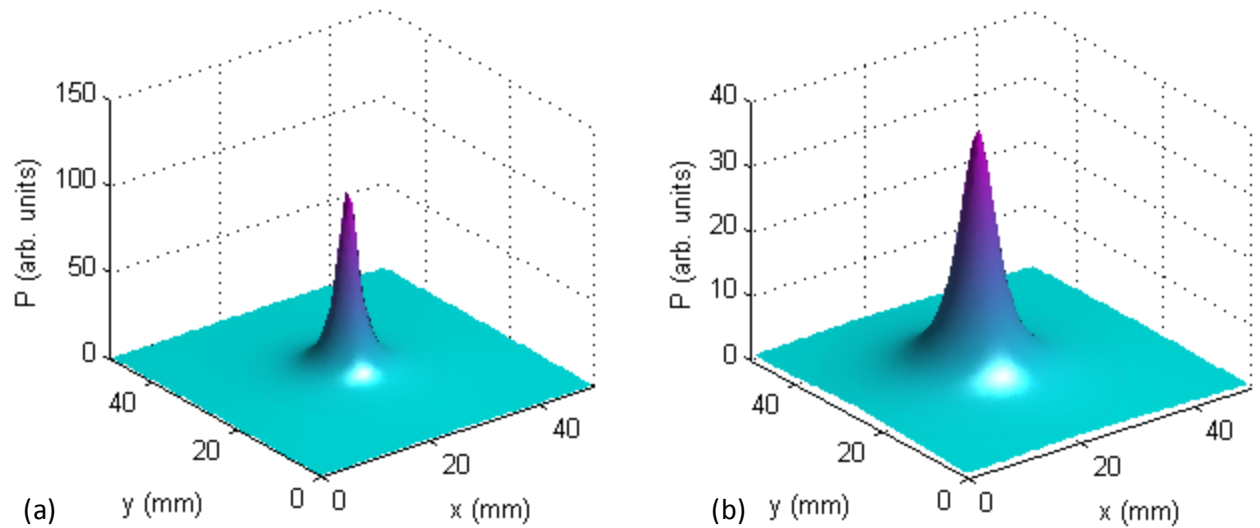


Fig. 3 TROT-reconstructed image at $z = 30.5$ mm using *fluorescence* data is shown in (a), and at $z = 29.5$ mm using transmission data shown in (b).

Table II. Known and retrieved target positions.

	Known	Retrieved	
		Fluorescence	Transmission
Position [x, y, z (mm)]	25.1, 25.7, 30.0	24.1, 25.6, 30.5	21.8, 25.6, 29.5
Error [$\Delta x, \Delta y, \Delta z$ (mm)]	-	1.0, 0.1, 0.5	3.3, 0.1, 0.5
FWHM [$\delta x, \delta y$ (mm)]	-	3.8, 3.8	6.9, 6.9

The transmission data was then analyzed for comparison. The target was also detected and its retrieved location is listed in Table I for comparison. The image of the target at $z = 29.5$ mm is shown in Fig. 3(b).

As shown in Table II, the location of target retrieved from the fluorescence data is in excellent agreement with the known position, and is consistent with that retrieved using transmission data. The pole of the pseudo image using fluorescence data is sharper than that obtained using transmission data. The FWHM of the pole in both x and y directions in the fluorescence-TROT image is 3.8 mm and 6.9 mm in the transmission-TROT image.

The results show that *fluorescence* TROT approach could detect and retrieve the locations of a small fluorescent target embedded in a breast-simulating turbid medium with the thickness comparable to that of a realistic compressed breast. The location of targets was retrieved with an accuracy of ~ 1 mm in all three dimensions. We plan to pursue this further for multiple targets.

5.4. Research Proposal Development

One of the proposed tasks (*Specific Aim 0, Task# 7*) involves developing at least one research proposal and submitting it to NIH or USAMRMC for funding. We submitted a pre-proposal entitled, “*Multimodal nanocomposites for detection and prevention of breast cancer metastases*” to the Idea Award (Collaborative Option) category of the 2012 Breast Cancer Research Program of CDMRP. S. K. Gayen (PI of this proposal) is the Initiating PI of the above-mentioned proposal. The Collaborative PI is Valeria Balogh-Nair of the CCNY Chemistry Department. A brief overview of the pre-proposal follows.

Research Idea

The *objective* of the proposed research is to develop multi-functional, tumor-targeting nanocomposites and near-infrared (NIR) optical imaging approaches for early detection of breast cancer, and prevention of micro-metastases that are responsible for majority of breast cancer mortality. The nanocomposite *synthesis* will use a multivalent dendrimer (a class of organic macromolecules) platform to incorporate fluorescent moieties (e.g., semiconductor quantum dots, or gold/silver nanoparticles) as contrast agents for *imaging*, and chemokine mimics for *selective targeting* of cancer cells and *prevention* of metastases. The high affinity of chemokine mimic’s ligands for chemokine CXCR4 receptors will ensure selective delivery of the nanocomposite to the target. A multi-source NIR probing and multi-detector signal acquisition arrangement along with a time-reversal image reconstruction algorithm will be used for fast detection of tumor and determination of its location in three dimensions.

Impact and Innovation

The *major impact* of the proposed research is that it has the potential to provide a modality for early detection of breast cancer, and for prevention of metastases, the major cause of mortality. A *broader potential impact* is that the approach could be extended to other cancers using chemokine mimics directed to other chemokine receptors.

The project is highly innovative in many ways. First, the synthesis process brings together the concept of multivalency, the idea of chemokine mimics for prevention of cancer cell migration, and use of dendrimers as stabilizers and nanoreactors for contrast agent synthesis. A combination of these novel ideas is proposed, to the best of our knowledge for the first time, as a multi-prong approach to fight the menace of breast cancer. Second, the affinity of the chemokine mimics to seven helix chemokine CXCR4 receptors obviates the need for a targeting vector. The chemokine mimics will play the dual role of: (1) “homing devices” for selective delivery of the nanocomposite to the tumor sites; and (2) “prevention agents” interacting with the chemokine receptor sites to inhibit metastases. Third, the efficacy of noninvasive NIR imaging approach for early detection and potential diagnosis will be significantly enhanced through design of efficient contrast agent. Fourth, the idea of time-reversal optical tomography (TROT) is a new paradigm in diffusive optical tomographic (DOT) imaging. While currently pursued DOT approaches are iterative and computation time intensive, TROT is non-iterative and will be faster, which is a necessary condition for real-time imaging. TROT is designed for detecting and locating small targets and will be suited for early detection when tumors are small. Finally, the dendrimer platform with multivalent surface will enable incorporation of moieties that enhance other imaging modalities, such as, magnetic resonance imaging, enabling development of sought-after dual or multimodal imaging modules.

6. KEY ACCOMPLISHMENTS

Key accomplishments include:

- (a) Development of a diffuse optical imaging approach based on decomposition methods (ICA, PCA and NMF), comparison of the performance of the three algorithms using experimental data on small tumor simulating targets embedded in breast simulating model media sample, and publication of the results in a peer-reviewed journal article;
- (b) Extension of Time Reversal Optical Tomography (TROT) (which is fast and minimally iterative) to extended targets and testing of its efficacy to locate the target and assess its size and optical strength using simulated data;
- (c) Initiating the development of the TROT formalism for fluorescent targets, and testing it for a single target in a breast phantom composed of a model medium that simulates the size and average optical properties of human breast;
- (d) Presentation of research results at the SPIE's International Symposium on Biomedical Optics, BiOS '12/ Photonics West, 21-26 January, 2012, San Francisco, California.
- (e) Recognition of the TROT formalism through its highlighting in "***Optics in 2012***" a special of the *Optics and Photonics News* (published by the Optical Society of America, December 2012). The OPN noted, "Bob Guenther, the guest editor of the issue, and a team of seven volunteer editors have combed through the work of scientists from around the globe to identify 30 summaries that highlight the most exciting optics research to emerge over the preceding 12 months." The journal article presenting our work on TROT ["Time reversal optical tomography: locating targets in a highly scattering turbid medium," *Opt. Express* **19**, 21956-21976 (2011)] was summarized for this special issue.
- (f) Development and submission of an independent research pre-proposal to BCRP 2012, an indication of the CCNY team's progress towards developing a sustainable breast cancer research program at CCNY.

7. REPORTABLE OUTCOMES

Publications

- (1) Binlin Wu, M. Alrubaiee, W. Cai, M. Xu, and S. K. Gayen, "Diffuse optical imaging using decomposition methods," *International J. Opt.* 2012, Article ID 185435, 12 pages (2012); doi:10.1155/2012/185435. (*Attached as Appendix 1*)
- (2) Binlin Wu, W. Cai, M. Xu, and S. K. Gayen, "Time-reversal optical tomography: detecting and locating extended targets in a turbid medium," *Proc. SPIE* Vol. 8216 82160K-1 – K-5 (2012), doi: 10.1117/12.906799 (*Attached as Appendix 2*)
- (3) Binlin Wu, Wei Cai, Swapan K. Gayen, "Time reversal optical tomography," *Optics and Photonics News* (OPN) special issue "Optics in 2012", December 2012, p. 41. Although the summary was published in the December 2012 issue of OPN, the source paper was published in 2011. So, we include it in this late report. (*Attached as Appendix 3*)

Conference Presentations

Binlin Wu, W. Cai, M. Alrubaii, M. Xu and S. K. Gayen, "Time-reversal optical tomography: detecting and locating extended targets in a turbid medium," Paper 8216-19 presented at the SPIE's International Symposium on Biomedical Optics, BiOS '12/ Photonics West, 21-26 January, 2012, San Francisco, California.

Research Proposal

S. K. Gayen (Initiating PI), V. Balogh-Nair (Collaborating PI), "*Multimodal nanocomposites for detection and prevention of breast cancer metastases*," submitted to the Idea Award (Collaborative Option) category of the 2012 Breast Cancer Research Program of CDMRP.

8. CONCLUSION

The work carried out during this reporting period: (a) shows the potential for noninvasive detection and three-dimensional localization of a tumor within a breast with significant accuracy based on the differences in the light scattering and absorption characteristics of the tumor and normal breast tissue; (b) presents the formalism and initial results of a fluorescence tomography approach that may provide higher contrast and better target identification based on molecular signatures and target selectivity of exogenous contrast agents.

“So What Section”

- The National Cancer Institute (NCI) has identified the development of imaging methodologies as an extraordinary opportunity for advancement in cancer research. Since the background of the CCNY team is in physical sciences and engineering, the training they received has provided them with necessary laboratory background in the biology of cancer research, and helping develop a knowledgeable multidisciplinary research force in the fight against breast cancer.
- A recent study involving 35,319 patients underscores the influence of primary tumor location on breast cancer prognosis [22], and makes it imperative that breast cancer detection modalities to obtain three-dimensional (3-D) location of the tumor relative to the axilla be developed. The optical imaging techniques (TROT, fluorescence TROT and other decomposition methods) being developed are an important steps in obtaining 3-D location of a tumor within the breast. The methods are minimally iterative, fast, and designed for locating small targets, which make those suitable for detecting tumors in early stages of development when those are more amenable to treatment.

9. REFERENCES

1. Annual Report Dated August 2008 covering the period 15 June 2007 – 14 June 2008, Award Number W81XWH-07-1-0454, on file at USAMRMC.
2. Annual Report Dated August 2009 covering the period 15 June 2008 – 14 June 2009, Award Number W81XWH-07-1-0454, on file at USAMRMC.
3. Annual Report Dated September 2010 covering the period 15 June 2009 – 14 June 2010, Award Number W81XWH-07-1-0454, on file at USAMRMC.
4. Annual Report Dated December 2011 covering the period 15 June 2010 – 14 June 2011, Award Number W81XWH-07-1-0454, on file at USAMRMC.

5. J. F. Cardoso, "Blind signal separation: statistical principle," *Proc IEEE* **86**, 2009-2025 (1998).
6. A. Hyvärinen, J. Karhunen, and E. Oja, *Independent Component Analysis* (Wiley, New York, 2001).
7. I. T. Jolliffe, *Principal Component Analysis* (Springer, New York, 1986).
8. M. W. Berry, M. Browne, A. N. Langville, V. P. Pauca, and R. J. Plemmons, "Algorithms and applications for approximate nonnegative matrix factorization," *Comp. Stat. Data Anal.* **52**, 155-173 (2007).
9. M. Xu, M. Alrubaiee, S. K. Gayen and R. R. Alfano, "Optical diffuse imaging of an *ex vivo* model cancerous human breast using independent component analysis," *IEEE J. Select. Topics Quantum Electron.* **14**, 43 (2008), and relevant references therein.
10. Binlin Wu, M. Alrubaiee, W. Cai, M. Xu, and S. K. Gayen, "Diffuse optical imaging using decomposition methods," *International J. Opt.* **2012**, Article ID 185435, 12 pages (2012); doi:10.1155/2012/185435.
11. Binlin Wu, W. Cai, M. Alrubaiee, M. Xu, and S. K. Gayen, "Time reversal optical tomography: locating targets in a highly scattering turbid medium," *Opt. Express* **19**, 21956-21976 (2011).
12. Hansen, P. C., "Analysis of discrete ill-posed problems by means of the L-curve," *Soc. Ind. Appl. Math. Rev.* **34**, 561-580 (1992).
13. Gruber, F. K. and Marengo, E. A., "Reinterpretation and enhancement of signal-subspace-based imaging methods for extended scatterers," *SIAM J. Imaging Sciences* **3**, 434-461 (2010).
14. B. P. Joshi and T. D. Wang, "Exogenous molecular probes for targeted imaging in cancer: focus on multi-modal imaging," *Cancers* **2**, 1251-1287 (2010).
15. A. Corlu, R. Choe, T. Durduran, M. A. Rosen, M. Schweiger, S. R. Arridge, M. D. Schnall, and A. G. Yodh, "Three-dimensional *in vivo* fluorescence diffuse optical tomography of breast cancer in humans," *Opt. Express* **15**, 6696-6716 (2007).
16. X. He, K. Wang, and Z. Cheng, "In *vivo* near-infrared fluorescence imaging of cancer with nanoparticle-based probes," *WIREs Nanomed. Nanobiotechnol.* **2**, 349-366 (2010).
17. S. Luo, E. Zhang, Y. Su, T. Cheng, and C. Shi, "A review of NIR dyes in cancer targeting and imaging," *Biomaterials* **32**, 7127-7138 (2011).
18. Y. Chen, X. Intes, and B. Chance, "Development of high-sensitivity near-infrared fluorescence imaging device for early cancer detection," *Biomed. Instrum. Technol.* **39**, 75-85 (2005).
19. V. Ntziachristos, J. Ripoll, and L. V. Wang, "Looking and listening to light: the evolution of whole-body photonic imaging," *Nat. Biotechnol.* **23**, 313-320 (2005).
20. A. B. Milstein, S. Oh, K. J. Webb, C. A. Bouman, Q. Zhang, D. A. Boas, and R. P. Millane, "Fluorescence optical diffusion tomography," *Appl. Opt.* **42**, 3081-3094 (2003).
21. H. J. van Staveren, C. J. M. Moes, J. van Marle, S. A. Prahl, and M. J. C. van Gemert, "Light scattering in Intralipid-10% in the wavelength range of 400--1100 nm," *Appl. Opt.* **31**, 4507-4514 (1991).
22. 16. N. Kroman, J. Wohlfahrt, H. T. Mouridsen, and M. Melbye, "Influence of tumor location on breast cancer prognosis," *Int. J. Cancer* **105**, 542 -545 (2003).

10. APPENDICES

Appendix 1. A reprint of: Binlin Wu, M. Alrubaiee, W. Cai, M. Xu, and S. K. Gayen, “Diffuse optical imaging using decomposition methods,” International J. Opt. **2012**, Article ID 185435, 12 pages (2012); doi:10.1155/2012/185435.

Appendix 2. A reprint of: Binlin Wu, W. Cai, M. Xu, and S. K. Gayen, “Time-reversal optical tomography: detecting and locating extended targets in a turbid medium,” Proc. SPIE Vol. 8216 82160K-1-K-5 (2012), doi: 10.1117/12.906799.

Appendix 3. A reprint of a summary article: Binlin Wu, Wei Cai, Swapan K. Gayen, “Time reversal optical tomography,” *Optics and Photonics News* (OPN) special issue “Optics in 2012”, December 2012, p. 41.

Appendix 1

Hindawi Publishing Corporation
International Journal of Optics
Volume 2012, Article ID 185435, 12 pages
doi:10.1155/2012/185435

Research Article

Diffuse Optical Imaging Using Decomposition Methods

Binlin Wu,¹ M. Alrubaiee,¹ W. Cai,¹ M. Xu,² and S. K. Gayen¹

¹Department of Physics, The City College and The Graduate Center of The City University of New York, 160 Convent Avenue, New York, NY 10031, USA

²Department of Physics, Fairfield University, 1073 North Benson Road, Fairfield, CT 06434, USA

Correspondence should be addressed to Binlin Wu, bwu@sci.ccny.cuny.edu

Received 25 September 2011; Revised 5 December 2011; Accepted 8 December 2011

Academic Editor: Baohong Yuan

Copyright © 2012 Binlin Wu et al. This is an open access article distributed under the Creative Commons Attribution License, which permits unrestricted use, distribution, and reproduction in any medium, provided the original work is properly cited.

Diffuse optical imaging (DOI) for detecting and locating targets in a highly scattering turbid medium is treated as a blind source separation (BSS) problem. Three matrix decomposition methods, independent component analysis (ICA), principal component analysis (PCA), and nonnegative matrix factorization (NMF) were used to study the DOI problem. The efficacy of resulting approaches was evaluated and compared using simulated and experimental data. Samples used in the experiments included Intralipid-10% or Intralipid-20% suspension in water as the medium with absorptive or scattering targets embedded.

1. Introduction

Diffuse optical imaging (DOI) for detection and retrieval of location information of targets in a highly scattering turbid medium may be treated as a blind source separation (BSS) problem [1, 2]. Various matrix decomposition methods, such as, independent component analysis (ICA) [3], principal component analysis (PCA) [4], and nonnegative matrix factorization (NMF) [5, 6] have been developed for solving the BSS problem and retrieving desired information.

Xu et al. adapted ICA of information theory to develop optical tomography using independent component analysis (OPTICA) and demonstrated its application for diffuse imaging of absorptive, scattering, and fluorescent targets [7–11]. ICA assumes the signals from different targets to be *independent* of each other and optimizes a relevant measure of independence to obtain the ICs associated with different targets. The position coordinates of targets in three dimensions are determined from the individual components separately.

PCA assumes that the PCs contributing to the signal are *uncorrelated* and explain the most variance in the signal. PCA has been widely used in various applications, such as spectroscopy [12], face recognition [13], and neuroimaging [14]. NMF seeks to factorize a matrix into two nonnegative matrices (component signals and weights) and requires the

contributions to signal and the weights of the components to be *non-negative*. It does not imply any relationship between the components. NMF has also been widely used in biological analysis [15] and spectral analysis [16].

The objective of this study is to test and compare the efficacy of these algorithms when used to solve the DOI problem. Results are presented and compared using simulative data and experimental data using absorptive and scattering targets embedded in model scattering media. Our interest in solving the DOI problem derives from the need for a noninvasive modality for detecting, locating, and diagnosing breast tumors in early stages of growth.

The remainder of the paper is organized as follows. In Section 2, the formalisms of the three methods are introduced. Section 3 evaluates the resulting imaging approaches using simulated data. The approaches are further examined in Section 4 for experimental data acquired using absorptive and scattering targets embedded in model scattering media. Section 5 summarizes and discusses the results.

2. Formalism

2.1. *Blind Source Separation Problem.* Blind source separation (BSS), also known as blind signal separation, is a general problem in information theory that seeks to separate different individual signals from the measured signals, which

are weighted mixtures of those individual signals. Assuming M individual signals, $s_j(t)$, $j = 1, \dots, M$, are linearly mixed instantaneously, the BSS problem is modeled as follows. The dimension of $s_j(t)$ is N_s , the number of sampling times. In this study, t will be replaced by spatial positions of the excitation light sources. A total of N_d detectors sense N_d different mixtures of $s_j(t)$. The mixture measured by the i th detector can be presented as $x_i(t) = \sum_{j=1}^M a_{ij} s_j(t)$, or $X = AS$, in a matrix notation, where $A \in R^{N_d \times M}$ is a mixing or weighting matrix, $S \in R^{M \times N_s}$, $X \in R^{N_d \times N_s}$, and $M < \min(N_s, N_d)$. The objective of BSS is to retrieve the signals $s_j(t)$ and their weights, a_{ij} . ICA, PCA, and NMF are statistical analysis methods used to solve the BSS problem.

2.2. Diffuse Optical Imaging Problem. In DOI, one measures the signal at the sample boundary, which includes a weighted mixture of contributions from embedded targets. One uses the diffusion approximation [17–19] of the radiative transfer equation [20, 21] as the forward model to describe light propagation in a highly scattering turbid medium. The perturbation in the light intensity distribution measured on the boundary of the sample due to the presence of the targets (which are localized inhomogeneities in the optical properties within the sample volume) may be written, in the first-order Born approximation, as [22, 23]

$$\Delta\phi(\mathbf{r}_d, \mathbf{r}_s) = - \int G(\mathbf{r}_d, \mathbf{r}) \delta\mu_a(\mathbf{r}) c G(\mathbf{r}, \mathbf{r}_s) d^3\mathbf{r} - \int \delta D(\mathbf{r}) c \nabla_{\mathbf{r}} G(\mathbf{r}_d, \mathbf{r}) \cdot \nabla_{\mathbf{r}} G(\mathbf{r}, \mathbf{r}_s) d^3\mathbf{r}, \quad (1)$$

where \mathbf{r}_s , \mathbf{r}_d , and \mathbf{r} are the positions of a source of unit power, detector and target, respectively; $G(\mathbf{r}, \mathbf{r}_s)$ and $G(\mathbf{r}_d, \mathbf{r})$ are the Green's functions that describe light propagation from the source to the target and from the target to the detector, respectively; $\delta\mu_a$ and δD are the differences in absorption coefficient and diffusion coefficient between the targets and the background medium, respectively; and c is the light speed in the medium.

A multisource illumination and multidetector signal acquisition scheme is used to acquire light transmitted through a scattering medium. For small absorptive targets, a perturbation data matrix is constructed using $-\Delta\phi$ for all sources. The elements of the data matrix pertaining to absorptive targets represented by the first term in (1) may be written in a discrete form as

$$X_{ij} = \sum_{m=1}^M G^d(\mathbf{r}_i, \mathbf{r}_m) \tau_m G^s(\mathbf{r}_m, \mathbf{r}_j) \quad (2)$$

$$(i = 1, 2, \dots, N_d; j = 1, 2, \dots, N_s),$$

where \mathbf{r}_i , \mathbf{r}_j , and \mathbf{r}_m are the locations of the i th detector, j th source and m th target, respectively; N_s , N_d , and M are the numbers of sources, detectors, and targets, respectively; $\tau_m = \delta\mu_a(\mathbf{r}_m) c \delta V_m$ is the optical absorption strength of the m th target of volume δV_m ; $G^s(\mathbf{r}_m, \mathbf{r}_j)$ and $G^d(\mathbf{r}_i, \mathbf{r}_m)$ are the Green's functions that describe light propagation from j th source to m th target and from m th target to i th detector,

respectively. The number of targets is assumed to be less than that of sources and detectors, $M < \min(N_d, N_s)$.

The m th target may be considered to be a virtual source of strength $\tau_m G^s(\mathbf{r}_m, \mathbf{r}_j)$ excited by the real light source located at \mathbf{r}_j . The data matrix $X = \{X_{ij}\}$ may be considered to be a set of combinations of light signals from all virtual sources mixed by a mixing matrix $\{G^d(\mathbf{r}_i, \mathbf{r}_m)\}$. Therefore, this problem can be treated as a BSS problem.

As the second term in (1) suggests, each scattering target is represented by three colocated virtual sources of strength: $\tau_m \partial_p G^s(\mathbf{r}_m, \mathbf{r}_j)$, where $\partial_p = \partial/\partial p$, ($p = x, y, z$), and $\tau_m = \delta D(\mathbf{r}_m) c \delta V_m$, is the optical scattering strength of the m th target [8]. The mixing matrices become $\{\partial_p G^d(\mathbf{r}_i, \mathbf{r}_m)\}$ for the three virtual sources generated by the m th target. The elements of the data matrix for scattering targets may be written as

$$X_{ij} = \sum_{m=1}^M \sum_{p=\{x,y,z\}} \partial_p G^d(\mathbf{r}_i, \mathbf{r}_m) \tau_m \partial_p G^s(\mathbf{r}_m, \mathbf{r}_j). \quad (3)$$

Since one absorptive target is represented by one centrosymmetric virtual source, while three virtual sources (one centrosymmetric and two dumb-bell shaped) represent one scattering target [7, 8], the number and patterns of virtual sources may be used, in favorable situations, to identify the target as absorptive or scattering in nature. In this paper, only small targets are considered since all three algorithms are suited for small targets, and early detection, when the tumors are more amenable to treatment, is of practical interest.

2.3. DOI as a BSS Problem. The data matrix for the DOI problem may be written as

$$X = AS = \sum_{m=1}^M A_{im} S_{mj}, \quad (4)$$

where $A \in R^{N_d \times M}$, $S \in R^{M \times N_s}$, and $X \in R^{N_d \times N_s}$. For absorptive targets,

$$A_{im} = \beta_m G^d(\mathbf{r}_i, \mathbf{r}_m), \quad S_{mj} = \alpha_m G^s(\mathbf{r}_m, \mathbf{r}_j), \quad (5a)$$

while for scattering targets,

$$A_{im} = \beta_m \partial_p G^d(\mathbf{r}_i, \mathbf{r}_m), \quad S_{mj} = \alpha_m \partial_p G^s(\mathbf{r}_m, \mathbf{r}_j). \quad (5b)$$

$\{S_{mj}\}$ ($j = 1, 2, \dots, N_s$) and $\{A_{im}\}$ ($i = 1, 2, \dots, N_d$) are two-dimensional intensity distributions on the source and detector planes, respectively. Source and detector planes are the boundaries of the sample through which light enters and exits the sample volume, respectively. The scaling factors β_m and α_m are related to the target optical strength, $\tau_m = \alpha_m \beta_m$.

Appendix 1

The location of the target and the scaling factors can be retrieved using a least squares fitting via

$$\underset{\alpha_m, \beta_m, \mathbf{r}_m}{\operatorname{argmin}} \left\{ \sum_j \left[\alpha_m^{-1} S_{mj} - G^s(\mathbf{r}_m, \mathbf{r}_j) \right]^2 + \sum_i \left[\beta_m^{-1} A_{im} - G^d(\mathbf{r}_i, \mathbf{r}_m) \right]^2 \right\}, \text{ or} \quad (6a)$$

$$\underset{\alpha_m, \beta_m, \mathbf{r}_m}{\operatorname{argmin}} \left\{ \sum_p \left\{ \sum_j \left[\alpha_m^{-1} S_{mj} - \partial_p G^s(\mathbf{r}_m, \mathbf{r}_j) \right]^2 + \sum_i \left[\beta_m^{-1} A_{im} - \partial_p G^d(\mathbf{r}_i, \mathbf{r}_m) \right]^2 \right\} \right\}, \quad (6b)$$

for absorptive and scattering targets, respectively. However, when a scattering target is embedded deep in a turbid medium, only the $\tau_m \partial_z G^s(\mathbf{r}_m, \mathbf{r}_j)$ virtual source remains significant. So, only $p = z$ may be used for fitting in (6b) [8].

2.3.1. ICA. OPTICA assumes that the virtual sources are *independent* of each other [8]. So, they can be retrieved through an iterative process which seeks to maximize the independence among the components. In practice, the independent components are found by maximizing some measure of non-Gaussianity, such as kurtosis (the fourth-order cumulant), of the unmixed components. A Matlab program for ICA was adopted from <http://sccn.ucsd.edu/eeglab/>. The location of the target can be retrieved by fitting the independent component intensity distributions (ICIDs) to Green's functions or derivatives of Green's functions using (6a) and (6b).

2.3.2. PCA. PCA assumes that the virtual sources are uncorrelated so that the correlation (covariance) between them is ideally zero and minimal in practice. The covariance matrix of S , $\text{cov}(S)$ should be diagonal. The general process of PCA is as follows. The data matrix $X = AS + \mathcal{N}$, where \mathcal{N} is random noise added to the data, A and S the same as defined in (4). When S is mean centered, elements of the mean-centered matrix S' are defined as

$$S'_{mj} = S_{mj} - \frac{1}{N_s} \sum_{j=1}^{N_s} S_{mj}. \quad (7a)$$

Similarly,

$$X'_{ij} = X_{ij} - \frac{1}{N_s} \sum_{j=1}^{N_s} X_{ij}. \quad (7b)$$

PCA looks for a matrix P that decomposes X into virtual sources, $S = PX$. It also holds that $S' = PX'$, since P is just a rotation matrix which does not change the center of the data.

$$\text{cov}(S) = S'S'^T = (PX')(PX')^T = PX'X'^TP^T = \Lambda, \quad (8)$$

where $\Lambda = \text{diag}\{\lambda_1, \lambda_2, \dots\}$. The eigenvalues λ_m are variances in the covariance matrix. Therefore, $X'X'^TP^T = P^T\Lambda$, where P^T is orthonormal. PCA is realized by eigenvalue decomposition (EVD) of the covariance matrix of X . The eigenvectors with leading eigenvalues (largest variances) are selected to be the PCs using the *L-curve* [24].

Since $X = P^T S \approx AS$, A is determined as a matrix including only PCs. S is calculated as $S \approx (A^T A)^{-1} A^T X$. Rows of S and columns of A represent principal component intensity distributions (PCIDs) on the source plane and detector plane, respectively and are proportional to the images of the virtual sources projected on the source and detector planes. The target positions are determined using (6a) and (6b).

2.3.3. NMF. NMF is a group of multivariate analysis algorithms that factorize a matrix X into A , and $S : X = AS$, A and S are nonnegative [6]. Unlike ICA and PCA, NMF does not imply any relationship between the retrieved components; instead, it just enforces non-negativity constraints on A and S . There are various algorithms developed to solve NMF, such as the multiplicative update method [5] and alternating least squares method [25, 26].

In the multiplicative update implementation of NMF, A and S can be found by minimizing the square of Euclidean distance $\|X - AS\|^2$ as the cost function, where $A \geq 0$ and $S \geq 0$, using the multiplicative update rule:

$$A_{ik} \leftarrow A_{ik} \frac{(XS^T)_{ik}}{(ASS^T)_{ik}}, \quad (9a)$$

$$S_{kj} \leftarrow S_{kj} \frac{(A^T X)_{kj}}{(A^T AS)_{kj}}. \quad (9b)$$

The alternating least squares implementation of NMF uses alternate least squares steps to estimate A (or S), and use that estimate to optimize S (or A), repeating the alternative steps until the desired optimization is obtained. Nonnegativity is ensured by setting any negative element of A or S equal to 0.

An NMF toolbox was obtained from <http://cogsys.imm.dtu.dk/toolbox/> to perform NMF computation. A built-in command *nnmf* is also available in Matlab (R2011a).

NMF algorithm requires that the non-negativity assumption must hold in the problem. In particular, for absorptive targets, when X is constructed with $-\Delta\phi$, τ_m should be positive, that is, the targets should be more absorbing than the background. If the targets have weaker attenuation properties than the background, X needs to be constructed with $+\Delta\phi$ instead. For scattering targets, X should be treated similarly to keep its elements positive.

When NMF is applied to a scattering target, only the centrosymmetric component shows up properly, since the other two components have dumb-bell shape which includes negative values [8]. So without any prior knowledge or some other experimental means to assess if the target is absorptive or scattering, NMF may not distinguish between the two possibilities.

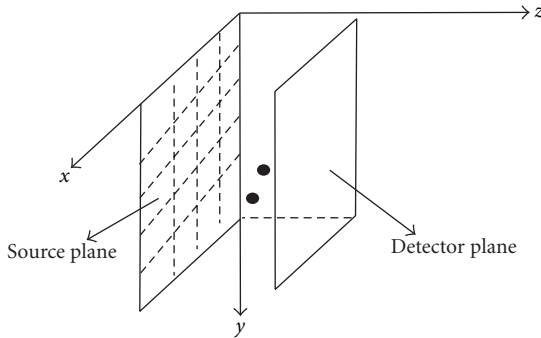


FIGURE 1: Light intensity distribution on the detector plane is recorded when a point source scans on the source plane.

The decomposition methods can be applied with different sample geometries such as slab and cylindrical geometries, and different measurement domains such as time-resolved domain, frequency domain, and continuous wave (CW). In this paper, Green's functions for slab geometry [23] with CW measurement were used for simulation and experiments.

3. Simulation

The sample was considered to be a 40 mm thick uniform scattering slab with lateral dimension of 80 mm \times 80 mm, as shown in Figure 1. Its absorption and diffusion coefficients were taken to be $\mu_a = 0.003 \text{ mm}^{-1}$ and $D = 1/3 \text{ mm}$ (transport mean free path, $l_t = 1 \text{ mm}$), respectively, which are similar to the average value of those parameters for human breast tissue. An absorptive and a scattering point targets were placed at (50, 60, 15) mm and (30, 30, 25) mm, respectively. The index of refraction n of the medium was taken to be 1.33. The speed of light is $2.998 \times 10^8 \text{ m/s}$ or 299.8 mm/ns in vacuum, and 225.4 mm/ns in the medium. The absorption coefficient of the absorptive target was set to be higher than the background with $\Delta\mu_a = 0.001 \text{ mm}^{-1}$, while the diffusion coefficient was taken to be the same as that of background. The diffusion coefficient of the scattering target was set to be lower than the background (higher scattering coefficient) with $\Delta D = -0.1 \text{ mm}$ ($l_t = 0.7 \text{ mm}$), while the absorption coefficient was taken to be the same as that of the background. The volumes of both targets are set to be 8 mm^3 . The optical strengths of the absorptive and scattering targets were $\Delta\mu_a c \Delta V = 1.803 \text{ mm}^3/\text{ns}$ and $\Delta D c \Delta V = -180.3 \text{ mm}^5/\text{ns}$, respectively. The incident CW beam step scanned the sample at 21×21 grid points covering an $80 \times 80 \text{ mm}^2$ area, with a step size of 4 mm. Light on the opposite side was recorded at 41×41 grid points covering the same area. Multiplicative Gaussian noise of 5% was added to the simulated data. The data matrix X was then obtained using (2) and (3) directly and analyzed using the three different algorithms.

3.1. ICA Analysis. One independent component for the absorptive target and three independent components for the scattering target were retrieved by ICA. The independent component intensity distributions (ICIDs) on the detector

plane are shown in Figures 2(a), 2(c), 2(d), and 2(e). Similar ICIDs were obtained on the source plane. Figure 2(g) shows the centrosymmetric ICID for the scattering target, and Figure 2(i) shows the ICID for the absorptive target, on the source plane.

The components in either the detector plane or the source plane can, in principle, be used to extract position and optical strength of the target(s). However, in our experimental arrangement signal is collected by a 1024×1024 pixels CCD camera, while the source plane is scanned in an x - y array of points, which is much smaller than the number of pixels in the CCD camera. Consequently, the resolution in the detector plane is much better, and the data set more robust than the source side. So, we used the images on the detector plane for retrieving target information using experimental data. While it would not matter in simulation, to be consistent with experimental situations, we employed detector plane images when using simulated data as well for all three algorithms. Table 1 lists the locations and strengths of the absorptive and scattering targets retrieved by fitting the spatial intensity profile of the centrosymmetric components on the detector plane to Green's functions and derivatives of Green's functions using (6a) and (6b), respectively, as shown in Figures 2(b) and 2(f). Figures 2(h) and 2(j) show the corresponding fits to the profiles on the source plane.

3.2. PCA Analysis. Eigenvalue equation of the covariance matrix of X was solved. The eigenvalues found by PCA were sorted in a descending order. Figure 3 shows a plot of leading 20 eigenvalues on a logarithmic scale.

First four leading eigenvalues were selected for PCs. The corresponding PCIDs were calculated. The PCIDs on the detector plane are shown in Figure 4. Similar images for PCIDs on the source plane were obtained. The scattering target has one centrosymmetric (Figure 4(a)) component and two dumb-bell shaped (Figures 4(c) and 4(d)) components, while the absorptive target has only one component (Figure 4(e)).

Figures 4(b) and 4(f) show fits to the spatial intensity profile of the centrosymmetric component of the scattering target and that of the absorptive target, respectively, to retrieve the locations of the two targets. The locations and optical strengths of the targets retrieved by PCA are also shown in Table 1.

3.3. NMF Analysis. The mixing matrix and virtual sources were retrieved from the data matrix X using NMF as explained in Section 2.3.3. As in the other two approaches, only one component is extracted for the absorptive target. Since NMF has a non-negativity constraint, only the centrosymmetric component for the scattering target is obtained. Nonnegative component intensity distributions (NCIDs) on detector planes are shown in Figure 5. Similar images for NCIDs on source plane were also obtained using the virtual sources in S . The results are also shown in Table 1.

3.4. Results and Discussion. The positions and optical strengths of the targets retrieved by ICA, PCA, and NMF

Appendix 1

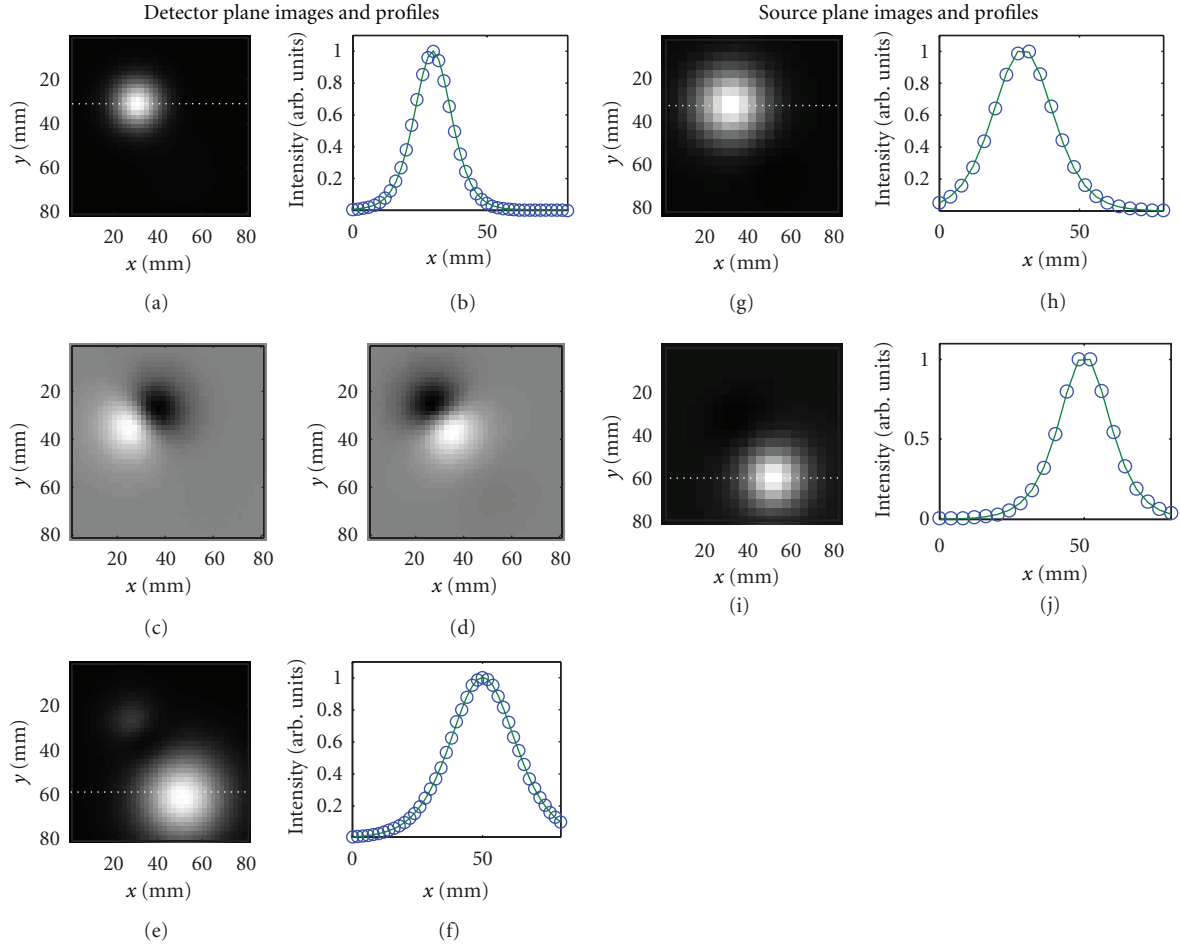


FIGURE 2: ICA-extracted two-dimensional intensity distribution on the detector plane of: (a) the centrosymmetric component; (c) and (d) dumb-bell shaped components of the scattering target; (e) the absorptive target. Similar intensity distribution on the source plane of: (g) the centrosymmetric component of the scattering target and (i) the absorptive target for comparison. Fits to the spatial intensity profile on the detector plane along the white dashed line (shown in figures) of the centrosymmetric component of the scattering target is shown in (b), and that of the absorptive target is shown in (f). Corresponding fits to spatial profiles on the source plane are displayed in (h) and (j), respectively.

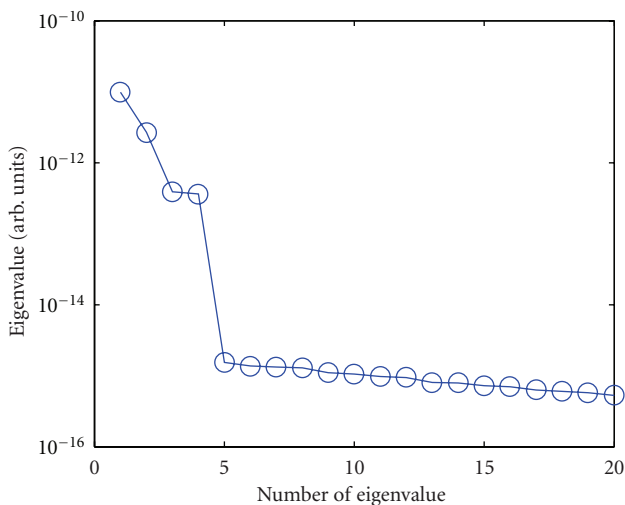


FIGURE 3: A logarithmic plot of the first 20 PCA eigenvalues.

algorithms are shown in Table 1, and compared to the known values. The retrieved results using all three algorithms from this simulated data are in excellent agreement with the known values.

4. Experiments

4.1. Experimental Materials and Methods. In this Section, the algorithms are evaluated using experimental data for absorptive and scattering targets embedded in model scattering media whose absorption and scattering properties are adjusted to mimic the average values of those parameters for human breast tissues. Two different experiments were carried out with two different samples. The first sample used a 250 mm \times 250 mm \times 50 mm transparent plastic container filled with Intralipid 10% suspension in water as the background medium. The concentration of Intralipid

TABLE 1: Positions and optical strengths retrieved using simulated data and ICA, PCA, and NMF algorithms.

Target	Known position (mm)	Algorithm	Fitted position (mm)	Error (mm)	Known strength*	Fitted strength*	Error (%)
Sca.	(30, 30, 25)	ICA	(29.9, 30.0, 25.1)	(0.1, 0, 0.1)	-180.3	-179.9	0.22
		PCA	(30.0, 30.0, 25.0)	(0, 0, 0)	-180.3	-180.1	0.11
		NMF	(30.0, 30.0, 25.0)	(0, 0, 0)	-180.3	-178.5	1
Abs.	(50, 60, 15)	ICA	(50.1, 60.2, 15.0)	(0.1, 0.2, 0)	1.803	1.826	1.28
		PCA	(50.1, 60.1, 14.9)	(0.1, 0.1, 0.1)	1.803	1.812	0.5
		NMF	(50.1, 60.1, 15.0)	(0.1, 0.1, 0)	1.803	1.803	0

*The unit for absorption strength of the target is mm^3/ns and for scattering strength is mm^5/ns .

10% was adjusted to provide [27, 28] an absorption coefficient of $\mu_a \sim 0.003 \text{ mm}^{-1}$, and a transport mean-free path $l_t \sim 1.43 \text{ mm}$ at 785 nm. The second sample used a similar container with dimension of 250 mm \times 250 mm \times 60 mm filled with Intralipid 20% suspension in water. The concentration of Intralipid 20% was adjusted to provide [27, 28] $\mu_a \sim 0.003 \text{ mm}^{-1}$, and $l_t \sim 1 \text{ mm}$ at 785 nm. These optical parameters of the medium were selected to be similar to the average values of those parameters for human breast tissue. The thickness of the samples was also comparable to that of a typical compressed female human breast.

In the first experiment, two absorptive targets were embedded in the medium. The targets were ~ 10 -mm diameter glass spheres filled Indocyanine green (ICG) dye dissolved in Intralipid-20% suspension in water to obtain an absorption coefficient $\mu_a = 1.15 \text{ mm}^{-1}$ at 785 nm, and to match the background scattering coefficient of 1.97 mm^{-1} . The targets were placed at (57.2, 18.1, 20.0) mm and (19.9, 48.1, 25.0) mm, respectively.

In the second experiment, two scattering targets were embedded, which were also ~ 10 mm diameter glass spheres, filled with Intralipid-20% suspension in water. The transport mean free path, l_t was adjusted to be 0.25 mm, with scattering coefficient $\mu_s \approx 11 \text{ mm}^{-1}$, and absorption coefficient μ_a same as that of the background medium. The targets were placed in the middle plane ($z = 30 \text{ mm}$) in the container with a lateral distance of 40 mm from each other (center to center).

The experimental setup is schematically shown in Figure 6. A 10 mW 785 nm diode laser beam was used to illuminate the first sample, while a 100 mW 785 nm diode laser beam was used for the second sample. The input surface (source plane) of the samples was scanned across the laser beam in an x - y array of grid points to realize the multi-source interrogation of the samples. The transmitted light from the exit surface (detector plane) was recorded by a 1024 pixel \times 1024 pixel (pixel size = $24 \mu\text{m}$) CCD camera (Photometrics CH350) equipped with a 60 mm focal-length camera lens. Each pixel of the CCD camera can be considered to be a detector implementing the multidetector signal acquisition arrangement. A set of 16 bit 1024 pixel \times 1024 pixel images were acquired. The two samples were scanned in an array of 11×12 and 11×15 grid points, respectively, with a step size of 5 mm in both cases. The processes of scanning and data acquisition were controlled by a personal computer. At all scan positions, raw transillumination images of the samples were recorded by the computer for further analysis.

4.2. Analysis and Results. A region of interest (ROI) was cropped out from each image. Then, every 5×5 pixels in each cropped image were binned to one pixel to enhance signal-to-noise ratio. A background image was generated by calculating an average image for all scan positions to approximate the transillumination image without target(s) embedded.

This averaging method for generating background image is suitable for small targets used in our experiments, as the ratio of the volume of the sample to that of the target was quite high ($\sim 500:1$). For *in vivo* imaging of tumors in early stages of growth, the breast-to-tumor volume ratio will be similarly high, and the averaging method will be applicable. Alternative approaches for generating a background image include using image of (a) a phantom that has the same average optical properties as the sample [29]; (b) the healthy contralateral breast for breast imaging [30]; (c) the sample obtained using light of wavelength for which the target(s) and the background have identical optical properties [31]. Still another approach is to compute the background using an appropriate forward model [32]. A more detailed discussion of this important issue appears in one of our earlier publications [33].

The background image was also cropped and binned corresponding to the ROI for each scan position. Perturbation in the light intensity distribution, $\Delta\phi$ due to targets in each image was found by subtracting the background image from the image. The data matrix X was then constructed using the light intensity perturbations at all scan positions. ICA, PCA, and NMF decomposition algorithms were performed on the data matrix separately. Results are shown and discussed below.

4.2.1. Absorptive Targets. The images on the detector plane obtained using the ICA, PCA, and NMF algorithms are shown in Figures 7, 8, and 9, respectively. Similar images on the source plane were also obtained using all three algorithms. The right side of each figure shows the corresponding spatial intensity profile. Locations of the targets are extracted from fits to these spatial intensity profiles, as described in Section 2.3 using (6a) and (6b). The results are presented in Table 2. In Figure 7, images on the source plane are shown in (e) and (g), and Green's function fits to their spatial profiles are shown in (f) and (h) for comparison.

It follows from the comparison of the results in Table 2 that the positions retrieved by all three algorithms are in good agreement with the known positions. The errors

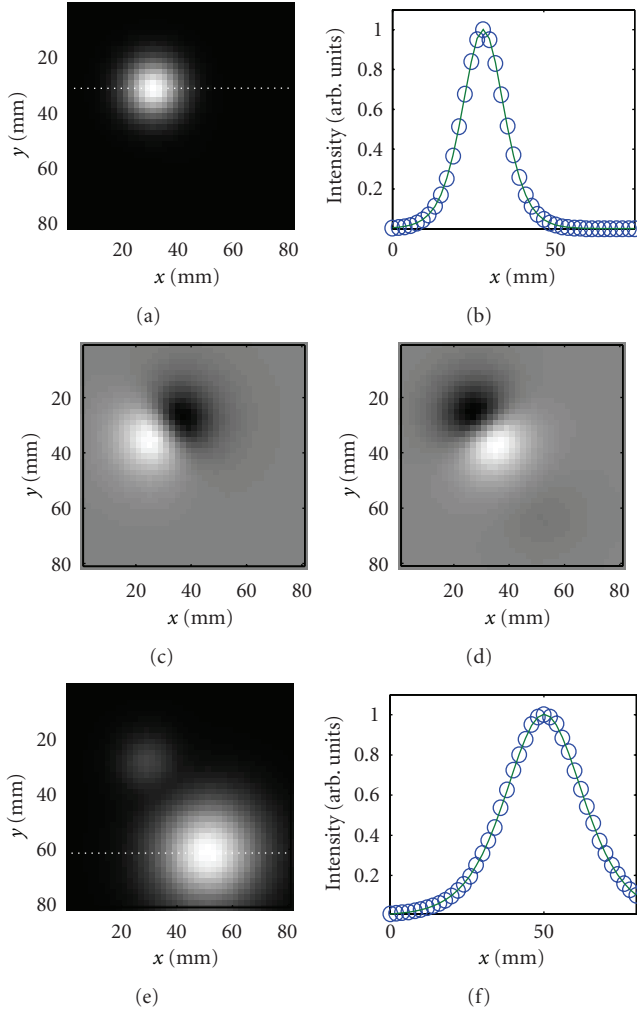


FIGURE 4: PCA-extracted two-dimensional intensity distribution on the detector plane of: (a) the centrosymmetric component; and (c) and (d) dumb-bell shaped components of the scattering target; (e) the absorptive target. Green's function fits to the spatial intensity profiles along the dashed line (shown in figures) of the (b) centrosymmetric component of the scattering target and (f) absorptive target, respectively, to retrieve the locations of the two targets.

in the retrieved locations (x, y, z) of the two targets were within 1.7 mm. The PCIDs were not totally separated. Some “residue” was observed in one PCID from the other. ICA and NMF separated two components from this dataset more clearly.

4.2.2. Scattering Targets. The “images” corresponding to the centrosymmetric components of the virtual sources (targets) on the detector plane obtained using the ICA, PCA, and NMF algorithms are shown in Figures 10, 11, and 12, respectively. Similar images on the source plane were also obtained. The right side of each figure shows the corresponding spatial intensity profile. Locations of the targets are extracted from fits to these spatial intensity

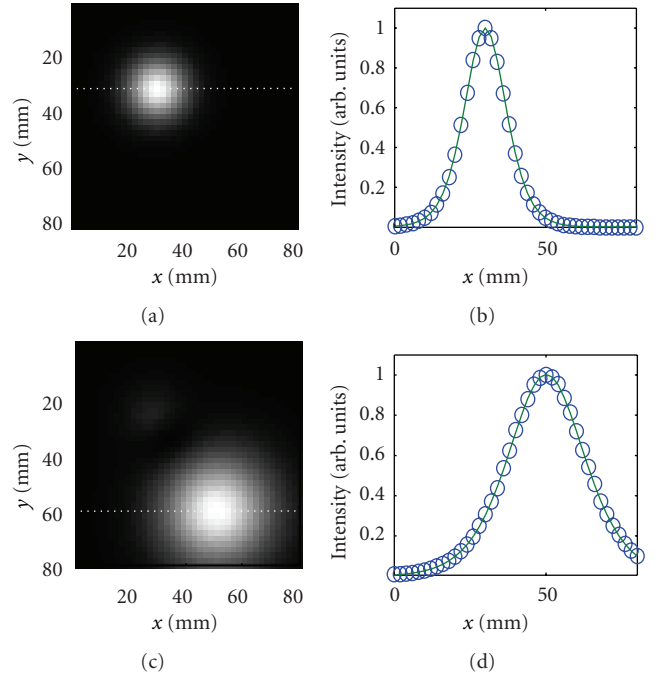


FIGURE 5: NMF-extracted two-dimensional intensity distribution on the detector plane of: (a) the centrosymmetric component of the scattering target; (c) the absorptive target. Fits to the corresponding spatial intensity profiles along the dashed line (shown in figures) are shown in (b) and (d), respectively.

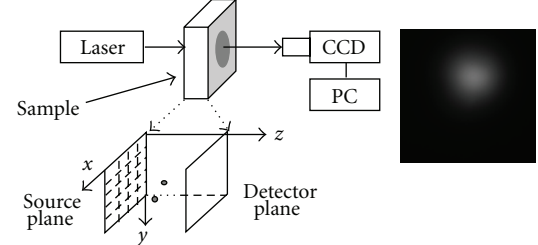


FIGURE 6: A schematic diagram of the experimental arrangement used for imaging objects embedded in a turbid medium. The inset at the bottom shows the 2D array in the input plane that was scanned across the incident laser beam; the inset to the right shows a typical raw image recorded by the CCD (CCD: charge coupled device, and PC: personal computer).

profiles, as described in Section 2.3 using (6a) and (6b). The results are presented in Table 3.

Both targets were detected by all three algorithms. The target locations retrieved by three algorithms are shown in Table 3 and compared with known locations. Overall, all three algorithms detect and locate the scattering and the absorptive targets with good accuracy, the maximum deviation of any one coordinate from the known value being ~ 3 mm. Since the maximum difference between the known and retrieved position coordinates was larger for the scattering targets, we calculated the squared correlation coefficient γ to assess the fitting quality. NMF retrieves

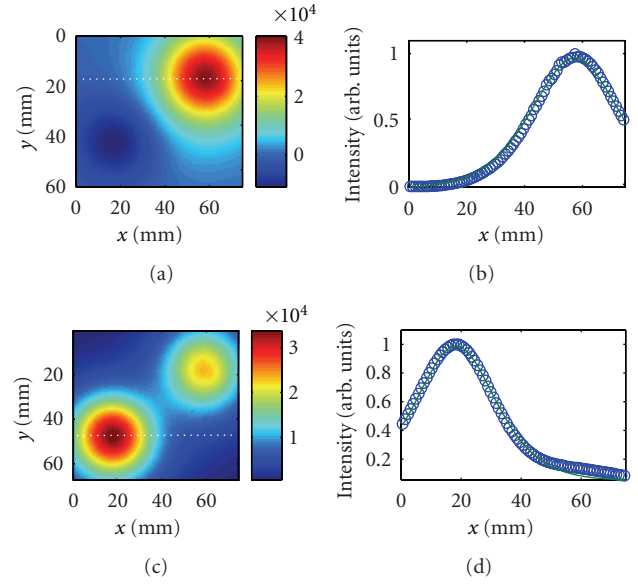
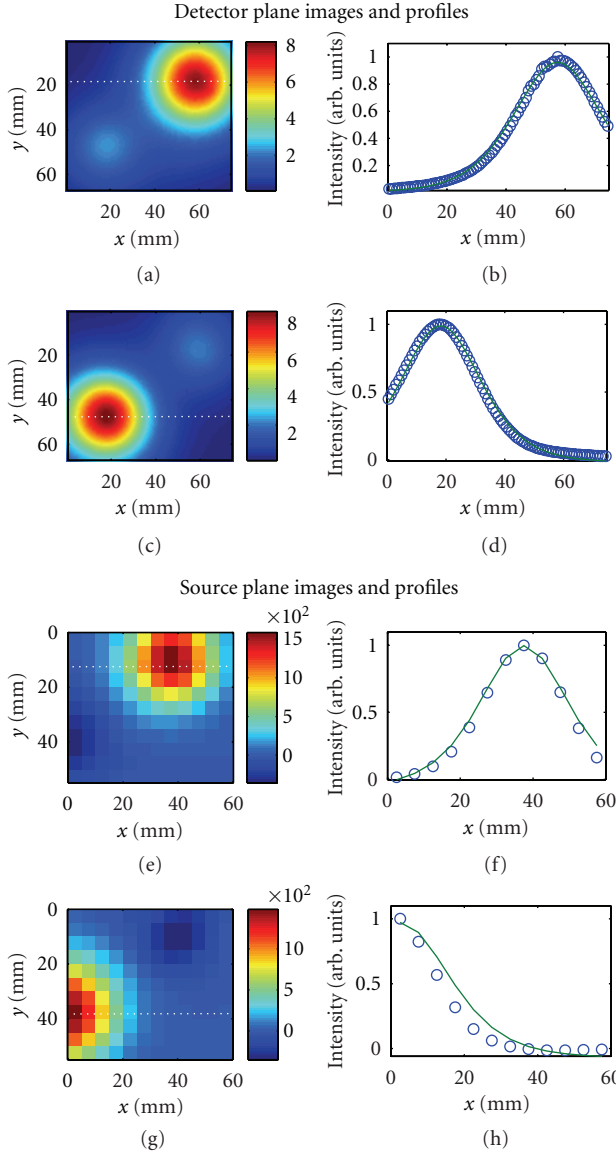


FIGURE 8: PCIDs on the detector plane are shown in (a) and (c); and corresponding Green's function fits to the horizontal spatial profiles through the dashed line are shown in (b) and (d).

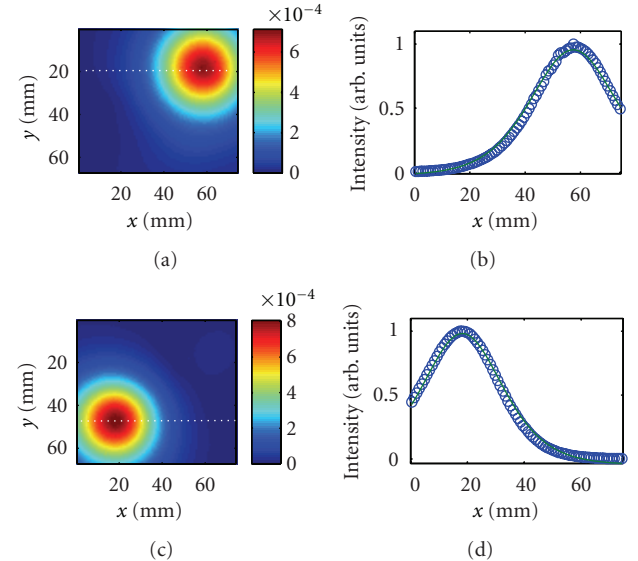


FIGURE 9: NCIDs on the detector plane are shown in (a) and (c); corresponding Green's function fits to the horizontal spatial profiles through the dashed line are shown in (b) and (d).

the position coordinates better (within 0.5 mm) for the scattering Target 2 than done by ICA and PCA (deviation from known values being between 2-3 mm). NMF retrieved the position coordinates for Target 1 with 3.0 mm error in z direction, which is not as good as that done by ICA and PCA. But γ is 0.783 and 0.778 in the fittings for ICA and PCA, respectively, as compared to 0.993 for NMF, indicating that the quality of the fitting is better for NMF. The quality of fitting is presumably affected by the efficacy of decomposition. The decomposed NCIDs by NMF were more “clean” than those decomposed by ICA and PCA. We ascribe the observed higher errors in ICA and PCA estimates of the

position coordinates of the scattering Target 2 than the NMF estimates to the interference from the other virtual source (corresponding to Target 1) in ICA (Figure 10(c)) and PCA (Figure 11(c)) images. It is commonly believed that errors in locating a scattering target are higher than that for locating an absorptive target, and the results of this study conform to that notion.

Appendix 1

TABLE 2: Known positions versus retrieved positions of the absorptive targets using ICA, PCA, and NMF algorithms.

Target	Known position (mm)	Algorithm	Fitted position (mm)	Error (mm)
1	(57.2, 18.1, 20)	ICA	(57.4, 18.2, 21.5)	(0.2, 0.1, 1.5)
		PCA	(57.4, 18.2, 20.6)	(0.2, 0.1, 0.6)
		NMF	(57.4, 18.2, 19.5)	(0.2, 0.1, 0.5)
2	(19.9, 48.1, 25)	ICA	(18.2, 46.7, 24.7)	(1.7, 1.4, 0.3)
		PCA	(18.2, 47.6, 25.9)	(1.7, 0.5, 0.9)
		NMF	(18.2, 47.6, 23.3)	(1.7, 0.5, 1.7)

TABLE 3: Known positions versus retrieved positions of the scattering targets using ICA, PCA, and NMF algorithms.

Target	Known position (mm)	Algorithm	Fitted position (mm)	Error (mm)
1	(13.0, 28.0, 30.0)	ICA	(12.6, 28.7, 29.1)	(0.4, 0.7, 0.9)
		PCA	(12.6, 28.7, 28.6)	(0.4, 0.7, 1.4)
		NMF	(12.0, 28.5, 33.0)	(1.0, 0.5, 3.0)
2	(53.3, 28.5, 30.0)	ICA	(51.0, 31.8, 26.8)	(2.3, 3.3, 3.2)
		PCA	(50.9, 31.8, 26.7)	(2.4, 3.3, 3.3)
		NMF	(53.3, 28.0, 30.3)	(0.0, 0.5, 0.3)

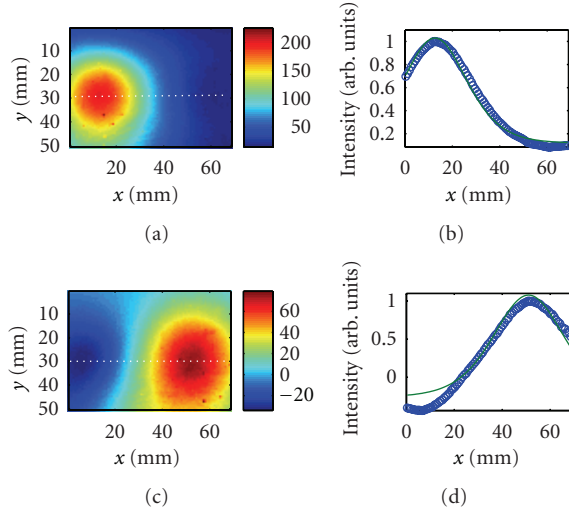


FIGURE 10: ICA-generated ICIDs on the detector plane are shown in (a) and (c); corresponding Green’s function fits to the horizontal spatial profiles through the dashed line are shown in (b) and (d).

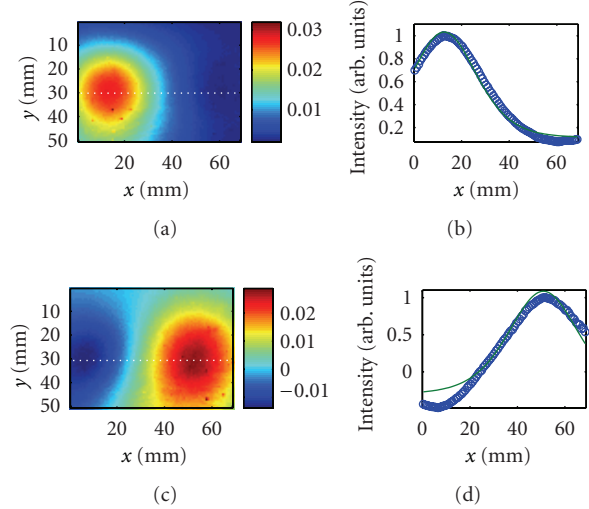


FIGURE 11: PCIDs on the detector plane are shown in (a) and (c); corresponding Green’s function fits to the horizontal spatial profiles through the dashed line are shown in (b) and (d).

5. Summary and Discussion

Diffusive optical imaging was modeled as a BSS problem. ICA, PCA, and NMF were used to decompose the data matrix and locate the targets embedded in a highly scattering turbid medium. Only the components corresponding to the targets were extracted from a large dataset for target detection and localization.

It may be instructive to compare the objectives, scope, and computational complexity of these decomposition methods with model-based reconstruction methods. Decomposition methods obtain the 3D locations of targets (the number of targets is generally small). Based on the retrieved locations, the methods may then be further

extended to retrieve size and optical property information of the targets [9]. The common practice of model-based inverse reconstruction methods is to discretize the sample volume into $N \times N \times N$ voxels and estimate absorption and/or scattering coefficient in each voxel iteratively. Voxels with significantly different optical properties than the surrounding are regions of interest and may be identified as targets. While estimating the optical properties, the forward model is solved repeatedly to calculate the intensity of the multiply scattered light on the sample boundary. The difference between the intensity of the multiply scattered light predicted by the forward model and the experimental measurements is minimized by seeking an optimal set of the optical properties of every voxel in the sample volume. The number of variables

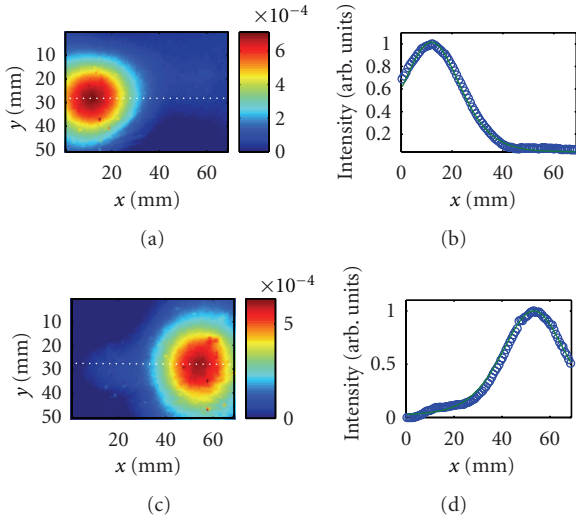


FIGURE 12: NCIDs on the detector plane are shown in (a) and (c); corresponding Green's function fits to the horizontal spatial profiles through the dashed line are shown in (b) and (d).

is thus, on the order of N^3 . To determine location(s) of target(s) in three dimensions, the decomposition methods process the data matrix to retrieve the main components (A and S). Here, A and S are two-dimensional matrices with the number of unknowns on the order of N^2 . The number of unknowns is, hence, reduced N times in the decomposition methods compared to the model-based approaches, which leads to a substantial saving in the computational time when N is large. No repeated solution of the forward model is involved in decomposition methods. Consequently, decomposition methods are considerably faster.

A comparison of the computational complexity of these two types of approaches may shed further light on their relative computation economy. For a model-based iterative reconstruction method, an equation of the form $b = Wx$ is solved to find the targets, where W is a weight matrix of size $N_d N_s \times N_v$, N_d , N_s , and N_v are the numbers of detectors, sources and voxels, respectively, b is an $N_d N_s \times 1$ vector describing the perturbation in the detected light intensity due to the presence of targets, and x is the perturbation in the optical properties from the background values with dimension of $N_v \times 1$. The computational complexity is typically $O(N_d N_s N_v^2)$ for a single iteration. For the decomposition approach, b is written as a 2D matrix X with dimension $N_d \times N_s$. To decompose matrix X , the computational complexity per iteration is typically of order $O(N_d N_k)$ for ICA [34], and $O(N_d N_s N_k)$ for NMF [16], where N_k is the number of components that relates to the number of targets and is usually a small number. For PCA using SVD, the complexity is $O(N_s^2 N_k)$ [34]. The computational complexity of the intrinsic iterative process involved in the matrix decomposition algorithms is much lower than that in the model-based inverse reconstruction methods.

All three matrix decomposition methods presented in this manuscript can potentially be used in *in-vivo* real-time breast cancer imaging. The three algorithms have

different assumptions, which may lead to different favored conditions. In this study, the algorithms were evaluated using simulative and experimental data using model scattering media and absorptive and scattering targets. The (x, y, z) positions of the targets were retrieved with good accuracy. The decomposition provided by ICA is “cleaner” than that of the PCA. PCA did not clearly separate the two absorptive targets used in the first experiment. NMF decomposition seems to provide residue-free “cleaner” images than the other two methods in this study. However, since NMF is based on nonnegativity assumption, the results might deteriorate when such a non-negativity assumption does not hold well. While continuous wave measurements were used in the work presented in this paper, the approaches could be used with frequency domain and time domain measurements as well.

The work presented here focuses on detecting and locating small targets, which derive impetus from the need to detect tumors in early stages of growth when those are more amenable to treatment. All three methods are applicable for extended targets as well and are expected to provide the “center of optical strength” as the location of the target.

All three approaches are applicable for both scattering and absorbing targets and may be used in clinical setting. The contrast between a tumor and surrounding normal tissue can be due to differences in absorption, scattering, or both absorption and scattering properties and may depend significantly on the wavelength of light used. However, *a priori* knowledge of the optical characteristics (absorptive or scattering) is not crucial. As has been shown in (2) and (3), the expression for elements of the data matrix for absorptive targets involves Green's Functions G , while that for scattering targets involves $\partial G / \partial z \approx -\kappa G$, where $\kappa = \sqrt{\mu_a / D}$ in CW [9]. This relationship with G provides basis for detection and localization of target(s), whether contrast is due to absorption, scattering, or both. We are using transillumination geometry, which is one of the approaches used by other researchers, and adequate signal for *in vivo* breast imaging is obtained [29, 35–38].

In this paper, we presented results when the approaches were used to detect and obtain three-dimensional location information of the targets. We have demonstrated, while developing OPTICA that a backprojection formalism can be further implemented to get a cross-section image of the target [11], or the retrieved target locations can be fed into other DOI methods as *a priori* information to get three-dimensional tomographic images. Since the approaches are suited for small targets, this hold promise for detecting and locating breast tumors in early stages of growth, which is crucially important for effective treatment. Further work involving *ex vivo* (model) and *in vivo* imaging of cancerous breast will be needed to establish the full potential of these approaches.

Acknowledgment

The paper is supported in part by US Army Medical Research and Materiel Command under Contract no. W81XWH-07-1-0454.

References

[1] X. R. Cao and R. W. Liu, "General approach to blind source separation," *IEEE Transactions on Signal Processing*, vol. 44, no. 3, pp. 562–571, 1996.

[2] J. F. Cardoso, "Blind signal separation: statistical principles," *Proceedings of the IEEE*, vol. 86, no. 10, pp. 2009–2025, 1998.

[3] A. Hyvärinen, J. Karhunen, and E. Oja, *Independent Component Analysis*, Wiley, New York, NY, USA, 2001.

[4] I. T. Jolliffe, *Principal Component Analysis*, Springer, New York, NY, USA, 1986.

[5] D. D. Lee and H. S. Seung, "Learning the parts of objects by non-negative matrix factorization," *Nature*, vol. 401, no. 6755, pp. 788–791, 1999.

[6] M. W. Berry, M. Browne, A. N. Langville, V. P. Pauca, and R. J. Plemmons, "Algorithms and applications for approximate nonnegative matrix factorization," *Computational Statistics and Data Analysis*, vol. 52, no. 1, pp. 155–173, 2007.

[7] M. Xu, M. Alrubaiee, S. K. Gayen, and R. R. Alfano, "Optical imaging of turbid media using independent component analysis: theory and simulation," *Journal of Biomedical Optics*, vol. 10, no. 5, Article ID 051705, 2005.

[8] M. Xu, M. Alrubaiee, S. K. Gayen, and R. R. Alfano, "Three-dimensional localization and optical imaging of objects in turbid media with independent component analysis," *Applied Optics*, vol. 44, no. 10, pp. 1889–1897, 2005.

[9] M. Xu, M. Alrubaiee, S. K. Gayen, and R. R. Alfano, "Optical diffuse imaging of an ex vivo model cancerous human breast using independent component analysis," *IEEE Journal on Selected Topics in Quantum Electronics*, vol. 14, no. 1, pp. 43–49, 2008.

[10] M. Alrubaiee, M. Xu, S. K. Gayen, M. Brito, and R. R. Alfano, "Three-dimensional optical tomographic imaging of scattering objects in tissue-simulating turbid media using independent component analysis," *Applied Physics Letters*, vol. 87, no. 19, Article ID 191112, pp. 1–3, 2005.

[11] M. Alrubaiee, M. Xu, S. K. Gayen, and R. R. Alfano, "Localization and cross section reconstruction of fluorescent targets in ex vivo breast tissue using independent component analysis," *Applied Physics Letters*, vol. 89, no. 13, Article ID 133902, 2006.

[12] D. L. Massart, B. G. M. Vandeginste, S. M. Deming, Y. Michotte, and L. Kaufman, *Chemometrics: A Textbook*, Elsevier, Amsterdam, The Netherlands, 1988.

[13] M. Turk and A. Pentland, "Eigenfaces for recognition," *Journal of Cognitive Neuroscience*, vol. 3, no. 1, pp. 71–86, 1991.

[14] L. K. Hansen, J. Larsen, F. A. Nielsen et al., "Generalizable patterns in neuroimaging: how many principal components?" *NeuroImage*, vol. 9, no. 5, pp. 534–544, 1999.

[15] J. P. Brunet, P. Tamayo, T. R. Golub, and J. P. Mesirov, "Metagenes and molecular pattern discovery using matrix factorization," *Proceedings of the National Academy of Sciences of the United States of America*, vol. 101, no. 12, pp. 4164–4169, 2004.

[16] V. P. Pauca, J. Piper, and R. J. Plemmons, "Nonnegative matrix factorization for spectral data analysis," *Linear Algebra and Its Applications*, vol. 416, no. 1, pp. 29–47, 2006.

[17] A. Ishimaru, "Diffusion of a pulse in densely distributed scatterers," *Journal of the Optical Society of America*, vol. 68, no. 8, pp. 1045–1050, 1978.

[18] K. Furutsu, "Diffusion equation derived from the space-time transport equation," *Journal of the Optical Society of America*, vol. 70, no. 4, pp. 360–366, 1980.

[19] M. S. Patterson, B. Chance, and B. C. Wilson, "Time resolved reflectance and transmittance for the non-invasive measurement of tissue optical properties," *Applied Optics*, vol. 28, no. 12, pp. 2331–2336, 1989.

[20] S. Chandrasekhar, *Radiative Transfer*, Clarendon Press, Oxford, UK, 1950.

[21] A. Ishimaru, *Wave Propagation and Scattering in Random Media*, vol. 1 of *Single Scattering and Transport Theory*, Academic, New York, NY, USA, 1978.

[22] S. R. Arridge and J. C. Schotland, "Optical tomography: forward and inverse problems," *Inverse Problems*, vol. 25, Article ID 123010, 2009.

[23] S. R. Arridge, "Photon-measurement density functions. Part I: analytical forms," *Applied Optics*, vol. 34, no. 31, pp. 7395–7409, 1995.

[24] P. C. Hansen, "Analysis of discrete ill-posed problems by means of the L-curve," *SIAM Review*, vol. 34, pp. 561–580, 1992.

[25] P. Paatero and U. Tapper, "Positive matrix factorization: a non-negative factor model with optimal utilization of error estimates of data values," *Environmetrics*, vol. 5, no. 2, pp. 111–126, 1994.

[26] P. Paatero, "The multilinear engine: a table-driven, least squares program for solving multilinear problems, including the n-way parallel factor analysis model," *Journal of Computational and Graphical Statistics*, vol. 8, no. 4, pp. 854–888, 1999.

[27] H. J. van Staveren, C. J. M. Moes, J. van Marle, S. A. Prahl, and M. J. C. van Gemert, "Light scattering in Intralipid-10% in the wavelength range of 400–1100 nm," *Applied Optics*, vol. 31, pp. 4507–4514, 1991.

[28] C. Bordier, C. Andraud, E. Charron, J. Lafait, M. Anastasiadou, and A. De Martino, "Illustration of a bimodal system in Intralipid-20% by polarized light scattering: experiments and modeling," *Applied Physics A*, vol. 94, no. 2, pp. 347–355, 2009.

[29] T. Nielsen, B. Brendel, R. Ziegler et al., "Linear image reconstruction for a diffuse optical mammography system in a noncompressed geometry using scattering fluid," *Applied Optics*, vol. 48, no. 10, pp. D1–D13, 2009.

[30] Y. Ardeshirpour, M. Huang, and Q. Zhu, "Effect of the chest wall on breast lesion reconstruction," *Journal of Biomedical Optics*, vol. 14, no. 4, p. 044005, 2009.

[31] B. W. Pogue, M. S. Patterson, H. Jiang, and K. D. Paulsen, "Initial assessment of a simple system for frequency domain diffuse optical tomography," *Physics in Medicine and Biology*, vol. 40, no. 10, pp. 1709–1729, 1995.

[32] A. Poellinger, J. C. Martin, S. L. Ponder et al., "Near-infrared laser computed tomography of the breast. First clinical experience," *Academic Radiology*, vol. 15, no. 12, pp. 1545–1553, 2008.

[33] B. Wu, W. Cai, M. Alrubaiee, M. Xu, and S. K. Gayen, "Time reversal optical tomography: locating targets in a highly scattering turbid medium," *Optics Express*, vol. 19, no. 22, pp. 21956–21976, 2011.

[34] T. Ristaniemi and J. Joutsensalo, "Advanced ICA-based receivers for block fading DS-CDMA channels," *Signal Processing*, vol. 82, no. 3, pp. 417–431, 2002.

[35] M. Cutler, "Transillumination as an aid in the diagnosis of breast lesions," *Surgery, Gynecology and Obstetrics*, vol. 48, pp. 721–729, 1929.

[36] R. Choe, A. Corlu, K. Lee et al., "Diffuse optical tomography of breast cancer during neoadjuvant chemotherapy: a case study with comparison to MRI," *Medical Physics*, vol. 32, no. 4, pp. 1128–1139, 2005.

[37] A. Pifferi, P. Taroni, A. Torricelli, F. Messina, R. Cubeddu, and G. Danesini, "Four-wavelength time-resolved optical

Appendix 1

mammography in the 680-980-nm range,” *Optics Letters*, vol. 28, no. 13, pp. 1138–1140, 2003.

[38] B. J. Tromberg, B. W. Pogue, K. D. Paulsen, A. G. Yodh, D. A. Boas, and A. E. Cerussi, “Assessing the future of diffuse optical imaging technologies for breast cancer management,” *Medical Physics*, vol. 35, no. 6, pp. 2443–2451, 2008.

Time-reversal optical tomography: detecting and locating extended targets in a turbid medium

Binlin Wu^{*ab}, W. Cai^a, M. Xu^c, and S. K. Gayen^{ab}

^aPhysics Department, The City College of the City University of New York, 160 Convent Ave, New York, NY 10031;

^bThe Graduate Center of the City University of New York, 365 Fifth Ave, New York, NY 10016, USA;

^cPhysics Department, Fairfield University, 1073 North Benson Road, Fairfield, CT 06824, USA

ABSTRACT

Time Reversal Optical Tomography (TROT) is developed to locate extended target(s) in a highly scattering turbid medium, and estimate their optical strength and size. The approach uses Diffusion Approximation of Radiative Transfer Equation for light propagation along with Time Reversal (TR) Multiple Signal Classification (MUSIC) scheme for signal and noise subspaces for assessment of target location. A MUSIC pseudo spectrum is calculated using the eigenvectors of the TR matrix T , whose poles provide target locations. Based on the pseudo spectrum contours, retrieval of target size is modeled as an optimization problem, using a “local contour” method. The eigenvalues of T are related to optical strengths of targets.

The efficacy of TROT to obtain location, size, and optical strength of one absorptive target, one scattering target, and two absorptive targets, all for different noise levels was tested using simulated data. Target locations were always accurately determined. Error in optical strength estimates was small even at 20% noise level. Target size and shape were more sensitive to noise. Results from simulated data demonstrate high potential for application of TROT in practical biomedical imaging applications.

Keywords: Diffuse optical imaging, time reversal, optical tomography, biomedical imaging, breast cancer, Multiple Signal Classification (MUSIC), near-infrared imaging

1. INTRODUCTION

Time Reversal Optical Tomography (TROT) has been developed [1] to detect and locate small targets embedded in highly scattering turbid media. The method was based on Diffusion Approximation of the Radiative Transfer Equation (RTE) to describe light propagation in a highly scattering turbid medium, and a Time Reversal (TR) Multiple-Signal-Classification (MUSIC) algorithm developed by other groups in acoustics and radar applications [2-7].

In this paper, we extend the TROT approach further to detect, locate and retrieve size and optical property information of extended targets embedded in a turbid medium. We test the formalism so developed using simulated data for a single absorptive target, a single scattering target, and two absorptive targets assuming different noise levels. This paper is organized as follows. Section 2 outlines the TROT formalism for extended targets. In section 3, simulated data, TROT analysis and results are presented. Section 5 serves as discussion and summary.

2. FORMALISM

TROT formalism for locating small (point-like) targets has been detailed in our earlier publication [1], and may be used to locate extended targets as well. Here we present a brief overview of the formalism for completeness, and outline how the size and optical strength of an extended target may be estimated. The propagation of a near-infrared (NIR) beam of light through a highly scattering turbid medium with embedded targets, whose optical properties are different from that of the intervening medium, may be approximated to be the diffuse transmission of light through background medium of uniform optical characteristics, with targets as perturbations. In the first order Born approximation, the perturbation in

*bwu@sci.ccny.cuny.edu; phone 1 212 650 5556

Appendix 2

the light intensity distribution due to the presence of the targets (inhomogeneities in optical properties) can be expressed using a data matrix [1] of the form:

$$K \approx \left\{ \sum_{m=1}^M G^d(\mathbf{r}_i, \mathbf{X}_m) \tau_m G^s(\mathbf{X}_m, \mathbf{r}_j) \right\} = \sum_{m=1}^M g_d(\mathbf{X}_m) \tau_m g_s^T(\mathbf{X}_m), \quad (1a)$$

for absorptive targets, and

$$K \approx \sum_{m=1}^M \sum_{\alpha \in \{x, y, z\}} \partial_\alpha g_d(\mathbf{X}_m) \tau_m \partial_\alpha g_s^T(\mathbf{X}_m), \quad (1b)$$

for scattering targets, where $g_s(\mathbf{r}) = \{G^s(\mathbf{r}, \mathbf{r}_j), j = 1, \dots, N_s\}$ and $g_d(\mathbf{r}) = \{G^d(\mathbf{r}_i, \mathbf{r}), i = 1, \dots, N_d\}$ are the Green's function vectors (GFVs) associated with the source and detector planes, respectively; the superscript T denotes transpose; $G^s(\mathbf{r}, \mathbf{r}_s)$ and $G^d(\mathbf{r}_d, \mathbf{r})$ are the Green's functions that describe light propagations in the background medium from a source at \mathbf{r}_s to a target (inhomogeneity) at \mathbf{r} and from the target to a detector at \mathbf{r}_d , respectively; $\tau_m = \delta\mu_a(\mathbf{X}_m) c \delta V_m$ ($\tau_m = \delta D(\mathbf{X}_m) c \delta V_m$) is the absorptive (scattering) optical strength of the m^{th} absorptive (scattering) target at \mathbf{X}_m with volume δV_m ; $\delta\mu_a$ (δD) is the difference in the absorption (diffusion) coefficients between the target and the background medium; N_s , N_d and M are the numbers of sources, detectors and targets, respectively. It is assumed the number of targets is less than the number of sources and detectors, $M < \min(N_d, N_s)$; c is the light speed in the medium. A time reversal matrix is constructed as $T_{SDDS} = K^T K$ [$T_{DSSD} = (K^T)^T K^T = K^* K^T$] in frequency domain, and $T_{SDDS} = K^T K$ ($T_{DSSD} = K K^T$) in the continuous wave illumination. T_{DSSD} and T_{SDDS} have a common set of eigenvalues $\{\lambda_j, j = 1, \dots, \min(N_s, N_d)\}$, and different sets of eigenvectors $\{u_i, i = 1, \dots, N_d\}$ and $\{v_j, j = 1, \dots, N_s\}$, respectively. The eigenvectors are separated into signal and noise subspaces using an L -curve method [8] with an eigenvalue threshold ε . For absorptive targets, the locations are determined using the MUSIC pseudo spectrum [1]

$$P_s(\mathbf{X}_p) = \left\| g_s(\mathbf{X}_p) \right\|^2 \left/ \left\| g_s(\mathbf{X}_p) \right\|^2 - \sum_{\lambda_j > \varepsilon} \left| v_j^T g_s(\mathbf{X}_p) \right|^2 \right\|, \quad (2a)$$

associated with the source plane or a similar form for the detector plane $P_d(\mathbf{X}_p)$, or the product of these two,

$$P(\mathbf{X}_p) = P_s(\mathbf{X}_p) P_d(\mathbf{X}_p), \quad (2b)$$

where \mathbf{X}_p is a test target position in the sample volume. Since the eigenvalues and eigenvectors of T_{SDDS} and T_{DSSD} can be connected using singular value decomposition (SVD), *i.e.*

$$K \approx \bar{U} \tilde{\Sigma} \bar{V}^T, \quad (3)$$

where $\bar{V} = \{v_j\}$ and $\bar{U} = \{u_i\}$, corresponding to $\tilde{\Sigma} = \text{diag}\{\sqrt{\lambda_j} > \varepsilon\}$, are matrices for the signal subspaces. By comparing Eq. (3) and Eq. (1), the target optical property can be retrieved by transforming the eigenvalue matrix $\tilde{\Sigma}$ via

$$\Gamma \approx (G^d)^{-1} \bar{U} \tilde{\Sigma} \bar{V}^T ((G^s)^T)^{-1}, \quad (4)$$

where $\Gamma = \text{diag}\{\tau_m, m = 1, \dots, M\}$; $G^s = \{g_s(\mathbf{r}_m)\}$, $G^d = \{g_d(\mathbf{r}_m)\}$ are matrices including GFVs associated with the retrieved target positions. For scattering targets, the GFVs g_d and g_s in Eqs. (2) and (4) are replaced by $\partial_\alpha g_d$ and $\partial_\alpha g_s$, $\alpha = x, y, z$, respectively.

An optimal contour (a surface Ω when plotted in 3D) in the pseudo spectrum in logarithmic scale is selected to be the boundary of the target(s), via [4]

$$\Omega = \arg \min_{\Omega} \|K - K_{\text{cal}}(\Omega)\|^2, \quad (5)$$

where K is normalized data matrix obtained from known target surface in simulation (from experimental measurements for real targets) and $K_{\text{cal}}(\Omega)$ is normalized data matrix calculated from the contour of the pseudo spectrum in logarithmic scale. The Green's functions used in the calculation are those for the intervening medium.

Appendix 2

3. SIMULATIONS AND ANALYSIS

The sample was taken to be a 40-mm thick uniform scattering slab with lateral dimension of 80 mm \times 80 mm. Its absorption and diffusion coefficients were assumed to be $\mu_a = 0.003 \text{ mm}^{-1}$ and $D = 1/3 \text{ mm}$ (transport mean free path, $l_t = 1 \text{ mm}$), respectively, which are similar to the average value of those parameters for human breast tissue. The index of refraction n of the medium was taken to be 1.33. The speed of light is $2.998 \times 10^8 \text{ m/s}$, or 299.8 mm/ns in vacuum, and 225.4 mm/ns in the medium. Three simulated datasets were generated with 10-mm diameter spherical targets embedded. In the first dataset, an absorptive target was centered at (40, 40, 20) mm. In the second dataset, two absorptive targets were located at (20, 40, 20) mm and (60, 40, 20) mm, respectively. In the third dataset, a scattering target was centered at (40, 40, 20) mm. The absorption coefficient of all the absorptive targets was set to be higher than the background with $\Delta\mu_a = 0.001 \text{ mm}^{-1}$, while the diffusion coefficient was taken to be the same as that of background. The diffusion coefficient of the scattering target was set to be lower than the background (higher scattering coefficient) with $\Delta D = -0.1 \text{ mm}$ ($l_t = 0.7 \text{ mm}$), while the absorption coefficient was taken to be the same as that of the background. The volume of all targets was 515 mm³ when the sample volume is discretized into 1 mm \times 1 mm \times 1 mm voxels in the forward model. The optical strength of the absorptive targets was $\Delta\mu_a c \Delta V = 116.08 \text{ mm}^3/\text{ns}$; while the optical strengths of the scattering target was $\Delta D c \Delta V = -11608.1 \text{ mm}^5/\text{ns}$. The incident CW beam step scanned the sample at 41 \times 41 grid points covering an 80 \times 80 mm² area, with a step size of 2 mm. Light on the opposite side was recorded at 41 \times 41 grid points covering the same area. Additive Gaussian noise of different noise levels was added to the simulated data. The data matrix K was then obtained using Eq. (1) directly, and analyzed using TROT. The results are shown below. For simplicity, when the reconstruction result for one target is displayed, a smaller volume of 40 mm \times 40 mm \times 40 mm around the center is selected. Due to the distortion in the retrieved target shape, target volume will be used to describe the target size.

3.1 One absorptive or scattering target

The first 20 eigenvalues of the TR matrix for one absorptive target with 20% added noise are plotted in logarithmic scale and shown in Fig. 1(a). The dimension of the signal subspace is determined to be 3. Using Eq. (2), the pseudo spectrum was calculated. Both of axial and sagittal views of the target using the pseudo spectrum are plotted in logarithmic scale in Figs. 1(b) and 1(c).

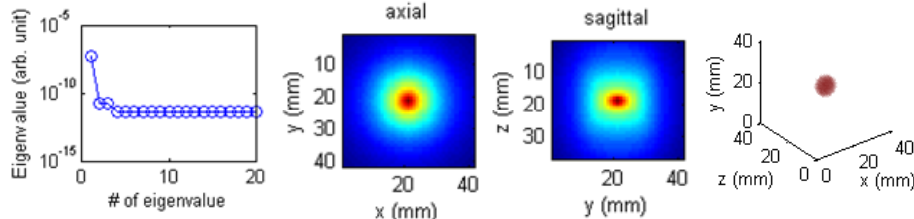


Fig. 1. (a) Eigenvalues plotted in logarithmic scale; (b) and (c) are the axial and sagittal views of the target using the pseudo spectrum in logarithmic scale; (d) is the retrieved target image

The center of the target was accurately determined to be (40, 40, 20) mm. Using Eq. (4), the optical strength was found to be 112.4 mm³/ns when all 3 eigenvalues and eigenvectors in the signal subspace were used, as shown in Table 1. We also found that if only the first eigenvalue and eigenvector in the signal subspace were used, the optical strength was found to be 112.4 mm³/ns as well. From this observation, we conclude that the property information of the extended target is mainly contained in the first eigenvalue, *i.e.* the number of the eigenvalues/eigenvectors used is the same as the number of targets.

Estimation of the target volume begins with choosing the optimal contour. Starting from the maximum of the pseudo spectrum, successive contour levels are selected. When a contour which is a surface \mathcal{Q} plotted in 3D, is selected, the volume enclosed inside \mathcal{Q} is assumed to be the target volume, and then the data matrix is calculated and compared with the working (simulated or experimental) data. When the next bigger volume is selected, only the signal generated by the extra volume dV is calculated. By using this “local contour” method [6], the optimal contour is found using Eq. (5). The reconstructed 3D image of the absorptive target is displayed in Fig. 1(d). The retrieved target volume is shown in Table 1 and compared with the known volume.

Similar simulated data was generated and the subsequent analysis was conducted when no noise, 5% noise, and 10% noise was added separately. Similar images were obtained (not shown). The target location and optical strength of the

Appendix 2

target was accurately retrieved in all cases. The size in all cases was also retrieved. The retrieved target optical strength and size are all shown in Table 1, and compared to the known values.

Similar simulations with one scattering target were carried out. The eigenvalues and eigenvectors of the TR matrix, and the pseudo spectrum were calculated. The target location of the scattering targets was accurately found to be (40, 40, 20) mm at all noise levels (0%, 5%, 10% and 20%). Axial and sagittal images of the scattering target were obtained using the pseudo spectrum as was done for the absorptive target. The scattering optical strength of the target was retrieved within 5.4% error and the size of targets was found within 30% error for all noise levels.

Further simulations show the optical strength can be retrieved even if the noise level is further increased or the target size and location vary; however, the error in the retrieved target size may increase dramatically if the target size further increases. The accuracy of the retrieved target size and optical property seems not to well correlate with the noise level.

Table 1. Optical strength and size of an absorptive target and a scattering target (10-mm diameter).

Noise Level (%)	Absorptive Target				Scattering Target			
	Optical Strength		Size		Optical Strength		Size	
	Retrieved (mm ³ /ns)	Error (%)	Retrieved (mm ³)	Error (%)	Retrieved (mm ⁵ /ns)	Error (%)	Retrieved (mm ³)	Error (%)
0	112.4	3.2	478	7.0	-10985.4	5.4	413	19.8
5	112.4	3.2	484	6.0	-10985.8	5.4	535	3.9
10	112.4	3.2	370	28.2	-10985.2	5.4	665	29.1
20	112.4	3.2	385	25.2	-10987.2	5.3	576	11.8

* Known values: volume: 515 mm³, absorptive optical strength: 116.08 mm³/ns, scattering optical strength: -11608.1 mm⁵/ns

3.2 Two absorptive targets

Next we considered the case of two spherical absorptive targets (diameter 10 mm) embedded in the medium, with a center-to-center separation of 40 mm. Different added noise levels: 0%, 5%, 10%, 20%, and 100% were considered. The eigenvalues and eigenvectors of the TR matrix, and the pseudo spectra were calculated. The target locations of two targets were accurately found to be (20, 40, 20) mm and (60, 40, 20) mm at all noise levels. Typical axial and sagittal images of the targets generated using the pseudo spectra for a noise level of 20% are displayed in Fig. 2. Similar images were obtained for other noise levels. The optical strength and size of both targets were found. The optical strength of each target was calculated within 3.3% error at all noise levels. The size of targets was found within 13.4% error when no noise was present, and varied with noise added. The retrieved optical strength and size of the targets are listed in Table 2 for different noise levels. Since both targets have the same optical property and size in the simulated data and the retrieved data, only one set of values is shown in the table.

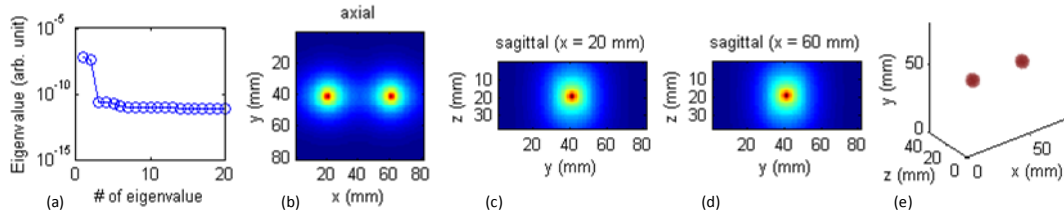


Fig. 2. (a) Eigenvalues plotted in logarithmic scale; (b), (c) and (d) are the axial and sagittal views of the targets using pseudo spectrum in logarithmic scale; (e) is the retrieved target image. The added noise level was 20%.

Further simulations (not shown here) indicate that retrieved target size was more accurate when small targets were involved. Simulations with one target at different locations and two targets with different separations were also tested for absorptive and scattering targets. The target locations were accurately retrieved in all of these cases. The retrieved optical strength in all cases was much less sensitive to the target location and size than the retrieved target size. As expected, it was more challenging to retrieve the optical strength and size of scattering targets than absorptive targets.

Further simulations also showed closer distance between two targets made target size retrieval more difficult, because of the cross talk between the two targets showing up in the contour of the pseudo spectrum (logarithmic scale).

Appendix 2

Table 2. Optical strength and size of two absorptive targets (10-mm diameter).

Noise Level (%)	Optical Strength		Size	
	Retrieved (mm ³ /ns)	Error (%)	Retrieved (mm ³)	Error (%)
0	112.3	3.3	584	13.4
5	112.3	3.3	295	42.7
10	112.3	3.3	368	28.5
20	112.3	3.3	487	5.4
100	112.2	3.3	663	28.7

* Known values: volume: 515 mm³, optical strength: 116.08 mm³/ns

4. SUMMARY AND DISCUSSION

Time reversal optical tomography (TROT) was further developed to deal with extended targets. The center position of the target(s) is determined rather accurately for both absorptive and scattering targets. It is found that the optical strength (absorption or scattering) can be retrieved for different target size, target location and noise level. However, it is much more challenging to retrieve the target size. The retrieved target size is determined by the details of the pseudo spectrum. There seems to be a lack of well defined correlation between the noise level and the size and optical strength of the targets, which needs to be understood. The efficacy of the approach will be further tested using experimental data.

ACKNOWLEDGEMENTS

The research is supported in part by USAMRMC under Contract Number W81XWH-07-1-0454.

REFERENCES

- [1] Wu, Binlin, Cai, W., Alrubaiee, M., Xu, M. and Gayen, S. K., "Time reversal optical tomography: locating targets in a highly scattering turbid medium," *Opt. Express* 19, 21956-21976 (2011).
- [2] Devaney, A. J., "Time reversal imaging of obscured targets from multistatic data," *IEEE Trans. Antenn. Propag.* 53, 1600-1610 (2005).
- [3] Fink, M., Cassereau, D., Derode, A., Prada, C., Roux, P., Tanter, M., Thomas, J. L. and Wu, F., "Time-reversed acoustics," *Rep. Prog. Phys.* 63, 1933-1995 (2000).
- [4] Gruber, F. K. and Marengo, E. A., "Reinterpretation and enhancement of signal-subspace-based imaging methods for extended scatterers," *SIAM J. Imaging Sciences* 3, 434-461 (2010).
- [5] Marengo, E. A., Gruber, F. K. and Simonetti, F., "Time reversal MUSIC imaging of extended targets," *IEEE Trans. Image Process.* 16, 1967-1984 (2007).
- [6] Hou, S., Solna, K. and Zhao, H., "Imaging of location and geometry for extended targets using the response matrix," *J. Comput. Phys.* 199, 317-338 (2004).
- [7] Hou, S., Solna, K. and Zhao, H., "A Direct Imaging Algorithm For Extended Targets," *Inverse Probl.* 22, 1151-1178 (2006).
- [8] Hansen, P. C., "Analysis of discrete ill-posed problems by means of the L-curve," *Soc. Ind. Appl. Math. Rev.* 34, 561-580 (1992).

OPTICAL COHERENCE TOMOGRAPHY

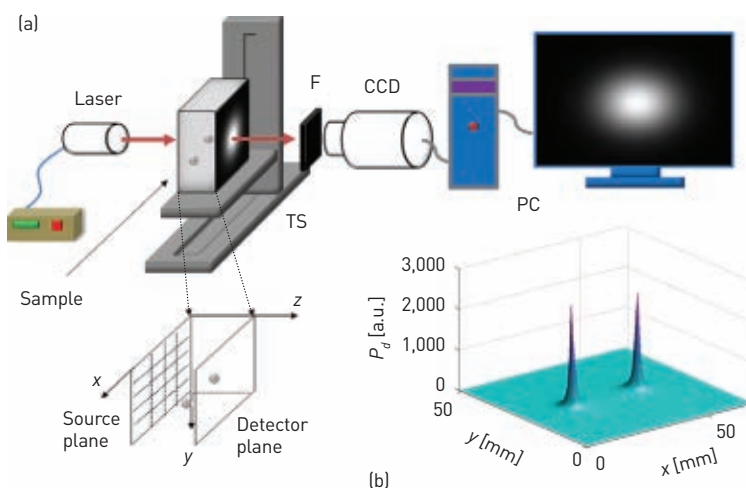
Time Reversal Optical Tomography

There has been a surge of interest in diffuse optical tomography (DOT) that uses near-infrared light to detect, localize and diagnose maladies such as breast cancer and brain injury.¹ Scattering and light attenuation limit the resolution and accuracy of DOT methods that use small differences in optical properties to distinguish lesions from normal tissue. Researchers need a DOT approach that can, for example, quickly reconstruct images to detect and map tumors at early growth stages and determine if they are malignant or benign.²

Time reversal optical tomography (TROT) extends the use of TR imaging and a subspace-based method of multiple signal classification (MUSIC) from acoustic and radar imaging to optical imaging.^{3,4,5} TROT uses a multisource illumination and multi-detector signal acquisition scheme to acquire multiple angular views of the sample.

The perturbation in light intensity distribution due to the targets is extracted from the data and organized in a matrix K . The leading eigenvalues of the TR matrix, $T = K^T K$, correspond to the targets whose locations are determined using MUSIC, along with Green's functions for light propagation in the sample.

We first tested the efficacy of TROT using a 60-mm-thick slab of Intralipid-20 percent suspension in water and 9-mm diameter glass spheres as absorptive or scattering targets. We filled the glass spheres with ink dissolved in the suspension to provide absorptive targets, and with a higher concentration of Intralipid to provide scattering targets. We chose the optical properties and size of the sample and targets to emulate average values for breast tissue and small



(a) F = signal transmitting narrow-band filter; TS = translation stage; CCD = charge coupled device; and PC = computer. Continuous wave 790-nm diode laser light illuminates the front of the sample cell. Diffusely transmitted light from the opposite face is collected by a camera lens through F and sensed by a CCD camera. The sample cell is step-scanned across the laser beam in a 2-D x-y array of grid points using the computer-controlled TS. (b) A TROT-generated pseudo image of two absorptive targets at $z = 30.5$ mm plane when the targets are separated by 27.6 mm.

tumors. We found that TROT could retrieve the location of a single target with millimeter accuracy and resolve two targets when their adjacent surfaces were only 4-mm apart.

Another experiment involved a realistic breast model composed of *ex vivo* breast tissue with two pieces of embedded tumors; TROT accurately located the positions of both the tumors. We have extended TROT for locating fluorescent targets.

TROT is non-iterative and faster than other iterative DOT approaches. It is particularly suited for detecting point-like targets. **OPN**

Researchers

Binlin Wu, Wei Cai and Swapan K. Gayen (gayen@sci.ccny.cuny.edu)
 City College and Graduate Center of the City University of New York, N.Y., U.S.A.

References

1. A.P. Gibson et al. *Phys. Med. Biol.* **50**, R1 (2005).
2. N. Kroman et al. *Int. J. Cancer* **105**, 542 (2003).
3. B. Wu et al. *Opt. Express* **19**, 21956 (2011).
4. M. Fink et al. *Rep. Prog. Phys.* **63**, 1933 (2000).
5. A.J. Devaney. *IEEE Trans. Antenn. Propag.* **53**, 1600 (2005).